



**UNIVERSITAT POLITÈCNICA DE CATALUNYA  
BARCELONATECH**

---

**Escola Tècnica Superior d'Enginyeria  
de Telecomunicació de Barcelona**

**LOW-NOISE MAGNETOMETER FOR SPACE  
EXPLORATION**

**A Master's Thesis**

**Submitted to the Faculty of the  
Escola Tècnica d'Enginyeria de Telecomunicació de  
Barcelona**

**Universitat Politècnica de Catalunya**

**by**

**Xavier Manyosa i Vilardell**

**In partial fulfilment  
of the requirements for the degree of  
MASTER IN ELECTRONICS ENGINEERING**

**Advisor: Manuel María Domínguez Pumar**

**Barcelona, December 2022**





**Title of the thesis:** Development of a miniaturized low-noise magnetometer for space missions

**Author:** Xavier Manyosa i Vilardell

**Advisor:** Manuel María Domínguez Pumar

## **Abstract**

The objective of this work is to develop a magnetic sensor, for space applications. Using magnetic field modulation with a MEMS resonator, it is possible to reduce the noise floor of a commercial Tunnelling Magnetic Resistor by two orders of magnitude, in the ultra-low frequency range. Low noise at this frequency range (below  $10 \text{ nT}/\sqrt{\text{Hz}}$ ) is a strong requirement in planetary or space exploration missions like LISA (Laser Interferometer Space Antenna), where the observed gravitational waves will be in the 0.1 mHz to 0.1 Hz range. It will be shown that the noise spectral amplitude after demodulation is below  $3 \text{ nT}/\sqrt{\text{Hz}}$  in the whole frequency range, and therefore the objectives of the project are fulfilled successfully.



This thesis is dedicated to my family and friends, who have celebrated with me every achievement during the master's degree and supported me during hard times. Specially I want to dedicate this degree thesis to my grandfather and my grandmother, who nowadays would be proud of my achievements, and this idea kept me studying and working hard during this degree and master, especially during the development of this project.



## **Acknowledgements**

I would like to express my deep and sincere gratitude to all the people who guided and helped me along the duration of this project. Specifically, I thank my research supervisor Professor Manuel M. Domínguez Pumar for introducing me to research, for teaching me many important concepts and for trusting me with this project. I also want to thank David Roma, Miquel Nofrarias and Juan Ramos, who also guided and helped me with their large experience and knowledge about magnetometers. To Joan Pons and Vicente Jimenez whose large experience and dedication helped me in many situations. To my laboratory colleague Nil Solà for providing very useful ideas and thoughts about the project. And to all the other people who has been related with this project, Marina Arqué, Víctor Martín, Josep Salvans and David Gascón.

It is critically important to say that this Thesis would have not been possible without the work of all the people listed, the outcome of this project and this thesis is the result of the collaborative work of all the people listed above and myself.



## Revision history and approval record

Revision	Date	Purpose
0	01/10/2022	Document creation
1	22/12/2022	Document revision

Written by:		Reviewed and approved by:	
Date	01/10/2022	Date	22/12/2022
Name	Xavier Manyosa i Vilardell	Name	Manuel Domínguez Pumar
Position	Project Author	Position	Project Supervisor



## **Table of contents**

Abstract .....	1
Acknowledgements .....	3
Revision history and approval record.....	4
Table of contents .....	5
List of Figures .....	7
List of Tables .....	9
1. Introduction.....	10
1.1. Modulation of the magnetic field (Working principle).....	11
1.2. Work plan .....	12
1.2.1. Work packages.....	12
1.2.2. Milestones .....	14
1.2.3. Gantt diagram.....	14
1.3. Deviations from the initial plan.....	15
1.3.1. MEMS manufacturer problem .....	15
1.3.2. Electronics used for the final noise measurements .....	15
2. State of the art.....	16
2.1. TMR Sensor .....	16
2.2. MEMS .....	16
2.3. Applications .....	18
2.3.1. LISA .....	18
2.3.2. Planetary exploration.....	18
2.3.2.1. MARS.....	18
2.3.2.2. Others .....	19
2.3.3. Low Earth Orbit .....	19
2.3.3.1. LEO Satellites .....	19
2.3.3.2. Altitude and Orbit Control systems .....	19
2.3.3.3. Measuring Earths magnetism for geomagnetic and magnetospheric monitoring .....	19
2.3.4. Cold Atom interferometry.....	20
3. TMR .....	21
3.1. TMR Characterization.....	21
4. MEMS used.....	23
4.1. MEMS Characterization.....	27



5.	Project development.....	32
5.1.	Setup Components.....	32
5.1.1.	Mu-metal chamber.....	32
5.1.2.	Helmholtz Coils .....	32
5.1.3.	Vacuum chamber .....	<b>Error! Bookmark not defined.</b>
5.1.4.	Temperature and Humidity controlled chamber .....	33
5.2.	Alignment and mounting the system.....	34
5.2.1.	Magnetic Flux Concentrators.....	34
5.2.2.	High mu-material on MEMS.....	35
5.2.3.	System assembly and positioning.....	36
6.	Characterization electronic system .....	39
7.	Results .....	44
7.1.	Modulation Depth .....	44
7.2.	Noise measurements.....	46
7.2.1.	Atmospheric pressure.....	46
7.2.2.	Vacuum .....	47
7.3.	Device comparison .....	48
8.	Conclusions and future development.....	50
	Bibliography.....	51
	Appendices.....	53
	Glossary .....	67

## **List of Figures**

Figure 1: Scheme of the working principle of the modulation. ....	11
Figure 2: Schematic of a tunneling magnetic sensor operation principle. ....	16
Figure 3: Schematic of the MEMS different layers. ....	16
Figure 4: Left: Lisa orbit. Right: Scheme of the LISA measurement principle. ....	18
Figure 5: Image of the TMR9001 bare die. ....	21
Figure 6: Set-up for the sensor noise characterization. ....	22
Figure 7: Noise floor measurement of the sensor. ....	22
Figure 8: Layout of the PiezoMUMPS resonators fabricated. ....	23
Figure 9: 3D schematic of the PiezoMUMPS resonator models fabricated. Top: simple cantilever shape, with two sizes: model #1 (1 x 4 mm) and model #2 (0.75 x 4 mm). Bottom: model #3: cantilever with suspended mass of size 1.5 x 4 mm; mass size is 1.5 x 1 x 400 $\mu\text{m}$ ....	24
Figure 10: Results obtained from COMSOL FEM simulations of the MEMS cantilevers. The graphs show the displacement amplitude around the first mechanical resonant frequency obtained applying 1V AC to the device. Top graphs correspond to device #1 (simple cantilever) and bottom graphs correspond to device #3 (cantilever with suspended mass), each for two quality factors. ....	25
Figure 11: Manufactured die and device individualization. ....	25
Figure 12: MEMS cantilever with mu foil tape attached. ....	26
Figure 13: Model for the impedance response of the MEMS cantilever, from [25]. ....	27
Figure 14: Comparison of the impedance response of a MEMS cantilever with and without mu foil. ....	27
Figure 15: Vacuum chamber. ....	28
Figure 16: Impedance response of a MEMS cantilever with mu foil at different pressures. ....	29
Figure 17: Evolution with pressure of the resonant frequency and the maximum conductance. ....	30
Figure 18: Evolution with pressure of the damping losses ( $R_m$ ) and the quality ( $Q$ ) factors. ....	31
Figure 19: 3-layer mu-metal chamber. ....	32
Figure 20: Helmholtz coil schematic. ....	32
Figure 21: Commercial Helmholtz coil used. ....	33
Figure 22: Helmholtz coils developed to fit inside the mu-metal chamber. ....	33
Figure 23: Temperature and Humidity controlled chamber. ....	34
Figure 24: PCB with the TMR only (left), and after attaching the MFCs (right). ....	34
Figure 25: Sputtering (left) and evaporation (right) chambers ....	35

Figure 26: MEMS device in a PCB, with the wire-bonding and the mu-foil deposited..... 35

Figure 27: 3D schema of the assembly/positioning of the MEMS PCB and the TMR PCB.  
..... 36

Figure 28: Micropositioner used to fix the MEMS PCB board (a). 3D printed part to fix the  
TMR PB board and the micropositioner (b). Full alignment system mounted, with the 3D  
printed part, the micropositioner and both PCBs mounted (c). ..... 36

Figure 29: Frequency swept of the conductance used to detect the resonance frequency  
(a). Vacuum chamber used at UPC (b). Helmholtz coils used to create a homogeneous  
and controlled magnetic field (c). ..... 37

Figure 30: Both PCBs TMR + Magnetic Flux concentrators (left) and MEMS (right). Note  
that the holes for the future fixation of the system are circled in red. .... 38

Figure 31: (Left) picture taken with microscope of the glass rods and epoxy used to fixate  
the systems. (Right) UPC clean room where the system is mounted. .... 38

Figure 32: Fast Fourier Transform of both signals, without MEMS (blue) and with MEMS  
modulating the signal (orange). Measurement used to obtain the modulation depth. .... 38

Figure 33: Developed analog board for the excitation of the MEMS and the acquisition of  
the signals. .... 39

Figure 34: Analog board schematic. .... 40

Figure 35: Digital operation of the system. .... 41

Figure 36: Diagram of needed functions for the PC application and for the STM23F401  
Firmware. .... 42

Figure 37: Timing diagram of the system. .... 43

Figure 38: MEMS conductance (Left), and Helmholtz coil (Right). .... 44

Figure 39: Vacuum chamber in UPC facilities. .... 45

Figure 40: Fast Fourier Transform of the measurements done with MEMS (orange) and  
without MEMS (blue), of a system that delivers 39% of modulation depth. .... 45

Figure 41: Spectral density of the sinus demodulation and cosine demodulation of a  
measure with the complete system..... 46

Figure 42: Vacuum chamber with mu-chamber inside (left). Vacuum chamber sealed (right).  
..... 47

Figure 43: Spectral density of the I/Q demodulation of a measurement with the complete  
system at vacuum..... 48



## **List of Tables**

Table 1: Comparison of the developed MEMS magnetometer to existing sensors for space exploration.....48

## 1. Introduction

Measurement of magnetic fields is a key issue for many science objectives in space exploration. At the surface of planetary bodies, static magnetic fields are typically measured for studying remnant paleo-magnetizations [1, 2] and for identifying the presence of magnetized rocks below the surface [3]. On the other hand, magnetic field fluctuations can generate disturbances in instruments where the signal to be retrieved is in the very low frequency range. This is the case of gravitational wave detectors, [4], as in the LISA mission (Laser Interferometer Space Antenna), or with the Very Broad Band (VBB) seismometer onboard InSight, [5]. Knowledge of the magnetic fluctuations can help to separate interfering signals from the signals of interest (gravitational or seismic waves, for example).

Additionally, very low frequency magnetic field fluctuations appear on the surface of planetary and minor bodies as a result of changes generated by the Interplanetary Magnetic Field (IMF), Solar wind, extreme UV radiation (EUV), or, alternatively, events generated by other planets (such as in the case of crossing another planet magneto-tail), [5, 6, 3]. All these phenomena trigger variations in the magnetic field at the surface of planets in a very low frequency range, and can, additionally, induce currents at the cores of the bodies themselves. By studying the transfer functions between the external excitations and the induced magnetic fluctuations it is possible to study the conductivity of the core and even its morphology [6]. The frequency range associated to all these fluctuations goes typically from  $10^{-5}$  or  $10^{-4}$ , to 0.1 Hz. This range represents a challenge for sensors and electronics because, in those low frequencies, the intrinsic  $1/f$  noise or the flicker noise, is the predominant issue when trying to have a low noise floor.

In order to reach these goals, the system presented in this work will be implementing magnetic field modulation over a Tunneling Magnetic Resistor (TMR). With this technique a high permeability material modulates the local magnetic field at the TMR, up-converting the signal to higher frequencies, [7, 8, 9, 10]. The objective of this paper is to show that it is possible to use this technique in the ultra-low frequency range needed in space exploration. In this work we are aiming to build a miniaturized and low magnetometer, achieving a noise amplitude spectral density (ASD) below  $10 \text{ nT}/\sqrt{\text{Hz}}$ , from 0.1 mHz to 100 mHz.

### 1.1. Modulation of the magnetic field (Working principle)

A magnetic field modulation has been implemented, in which the magnetic flux is sensed using TMRs, it is enhanced using MFCs (magnetic flux concentrators) layers, made from high magnetic permeability materials, and, a MEMS resonator is used to mechanically oscillate a MFC layer near the TMR [29]. Therefore, the magnetic flux sensed by the TMR is modulated to a higher frequency, therefore avoiding the low-frequency  $1/f$  noise which is predominant in the objective frequency range.

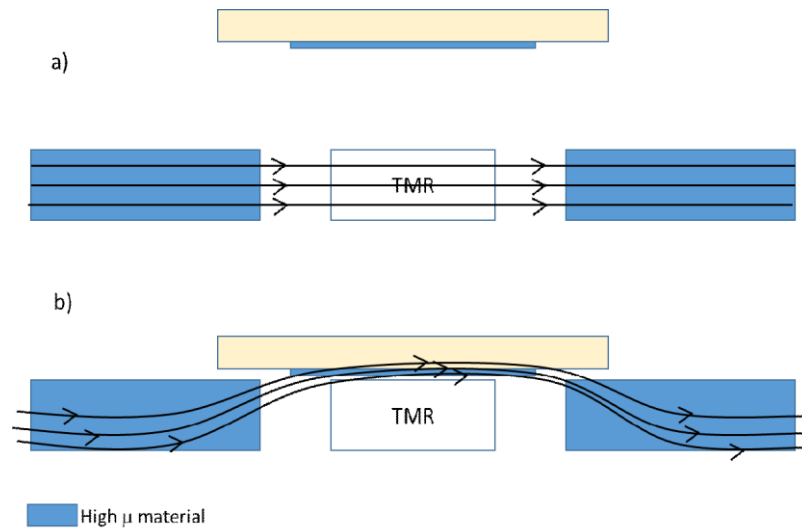


**Figure 1: Scheme of the working principle of the modulation.**

Fig. 1 illustrates the working principle of the system. In Fig. 1 a, it can be seen the effect of the system when the MFC layer is far away from the TMR, therefore the magnetic flux sensed by TMR is mostly unaffected by the MFC layer. In Fig. 1 b, when the MFC is near the TMR, the MFC mostly removes the magnetic flux sensed by the TMR.

Hence, the movement of the MEMS resonator allows to modulate the sensed magnetic flux, therefore pushing it to higher frequencies, where the  $1/f$  noise is reduced.

## 1.2. Work plan

In this chapter the work plan followed during the development of this project is explained, first, it describes the different work packages with its internal tasks, it is followed by the milestones reached and finally, a Gantt diagram is shown.

### 1.2.1. Work packages

Project: Development of a miniaturized low-noise magnetometer for space missions	WP ref: WP1	
Major constituent: State of the art study	Sheet 1 of 5	
Short description: Study the approach of the project. Study the mounting approach, study the state of the art, and understand it. Also learn the different techniques that will be used.	Planned months: 1-3	
	Months applied: 1-3	
Internal task T1: Study the state of the art, through reading multiple papers related to the project  Internal task T2: Study the possible applications, of the system that will be developed.  Internal task T3: Learn to apply the different techniques that will be used during the project. (PCB alignment, schematic, construction, 3D designs and printing...)		

Project: Development of a miniaturized low-noise magnetometer for space missions	WP ref: WP2	
Major constituent: Develop a first working concept and perform test iterations.	Sheet 2 of 5	
Short description: To develop a first system without using MEMS, by means of a simple and macro-cantilever system by using a piezoelectric actuator and a mu foil to modulate the signal.	Planned months: 4-8	
	Months applied: 4-8	
Internal task T1: Design the concept for the circuit  Internal task T2: Build the concept of the system  Internal task T3: Test the system concept, obtain modulation depths.		

Project: Development of a miniaturized low-noise magnetometer for space missions	WP ref: WP3	
Major constituent: Alignment and mounting design	Sheet 3 of 5	
Short description: Develop a system capable of aligning the MEMS and the TMR and to fixate them.	Planned months: 8-12	
	Months applied: 8-12	
Internal task T1: Design phase. PCB design, 3D models, drawings, tests, and fixation methods. Internal task T2: Build phase of the aligner.		

Project: Development of a miniaturized low-noise magnetometer for space missions	WP ref: WP4	
Major constituent: Electronic development	Sheet 4 of 5	
Short description: Develop a system capable of excitation of the MEMS at its resonance frequency and to acquire the signal from the TMR.	Planned months: 8-15	
	Months applied: 8-15	
Internal task T1: Design circuit schematics. Internal task T2: Build and test the circuit.		

Project: Development of a miniaturized low-noise magnetometer for space missions	WP ref: WP5	
Major constituent: Construction of the system and final noise measurements	Sheet 5 of 5	
Short description: Align and mount of multiple final systems and measure them to obtain the lowest noise possible.	Planned months: 12-19	
	Months applied: 12-19	
Internal task T1: Mount the systems Internal task T2: Characterize the system Internal task T3: Noise measurement of the system	Deliverables: Measurements	

### 1.2.2. Milestones

WP#	Task#	Short title	Date (Month)
WP1	T1	Study the state of the art	Month 1-2
	T2	Study possible applications	Month 2-3
	T3	Learn the different techniques	Month 2-3
WP2	T1	Concept design of the circuit	Month 4
	T2	Build of the concept design	Month 5
	T3	Test the system concept	Month 6-8
WP3	T1	Alignment system design phase	Month 8-10
	T2	Alignment system build phase	Month 10-12
WP4	T1	Design circuit schematics	Month 8-10
	T2	Build (PCB) and test of the circuit	Month 11-15
WP5	T1	Mount the systems	Month 12-14
	T2	Characterization of the system	Month 14-17
	T3	Noise measurement of the system	Month 18-19

### 1.2.3. Gantt diagram

Month	1	2	3	4	5	6	7	8	9	10	11	12	13	14	15	16	17	18	19
WP1.T1	█	█																	
WP1.T2		█	█																
WP1.T3		█	█																
WP2.T1				█															
WP2.T2					█														
WP2.T3						█	█	█											
WP3.T1								█	█	█									
WP3.T2									█	█	█								
WP4.T1								█	█	█									
WP4.T2											█	█	█	█	█				
WP5.T1												█	█	█					
WP5.T2													█	█	█	█			
WP5.T3																		█	█



### **1.3. Deviations from the initial plan**

#### **1.3.1. MEMS manufacturer problem**

Due to a specific problem occurred in the manufacturing of the batch (later recognized by the manufacturer), the devices showed leaks in the thermal oxide, which reduced the impedance of the MEMS, and made some devices not usable. Furthermore, the usable devices show brittleness with voltage stress, making it necessary to apply low voltages to preserve their durability.

In order to increase the displacement of the MEMS to have a viable system, without applying high voltages, the devices were mounted and tested at vacuum, where there is less air resistance, and therefore, a larger displacement of the MEMS is accomplished with a small voltage excitation.

#### **1.3.2. Electronics used for the final noise measurements**

At the end of the project, not enough tests could be done in order to fully trust the electronic system for the final noise measurements, anyway it was very useful and used during the assembly phase of the MEMS to detect modulation depths, and to check a correct behavior of the system. Therefore, another more thoroughly built and more characterized electronic system was adapted and used for the noise measurement, which was from the LETS project of the ICE (Institut Català del Espai).

## 2. State of the art

### 2.1. TMR Sensor

A Tunnelling Magnetic Resistor, is formed by multiple MTJ (Magnetic Tunneling Junction), formed by two ferromagnetic layers separated by a dielectric (Figure 2), one of the two layers has its spins pinned, and the other has the spins free, therefore they will orient in function of the external magnetic field. The up-spin electrons will only tunnel into up-spin states, and the down-spin electrons will only tunnel into the down-spin states. Therefore, when the magnetic flux is parallel to the pinned ferromagnetic layer, more electrons will tunnel through the dielectric, lowering the resistance of the device, and when the magnetic flux is antiparallel to the pinned layer, less electrons will tunnel through the dielectric, resulting in a higher resistance of the device.

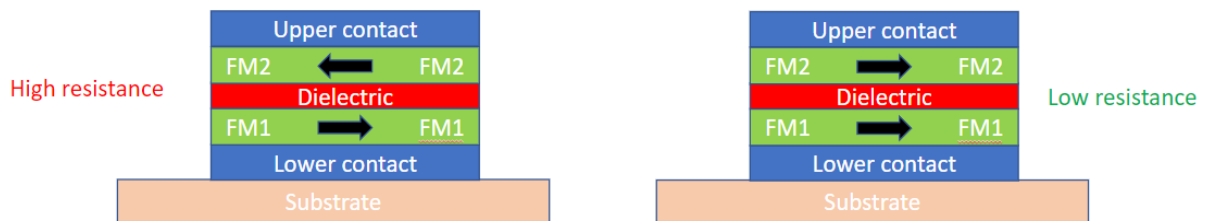


**Figure 2: Schematic of a tunneling magnetic sensor operation principle.**

### 2.2. MEMS

Various factors converged in the choice of technology, type and geometry of the designed MEMS resonators. On the one hand, the TMR magnetic sensors used have areas of 1.5 x 1 mm. Thus, the resonator must be a millimetric device, capable of "moving" a deposited layer of mu-metal of comparable dimensions, with oscillation frequencies below 1 KHz and amplitudes of the order of hundreds of microns. Additionally, the lowest possible actuation voltages are required (of the order of volts or a few tens of volts). On the other hand, due to the temporary restrictions of the project, accessibility and previous experience from other members of the team are also important factors in the choice of the technology used: PiezoMUMPS.

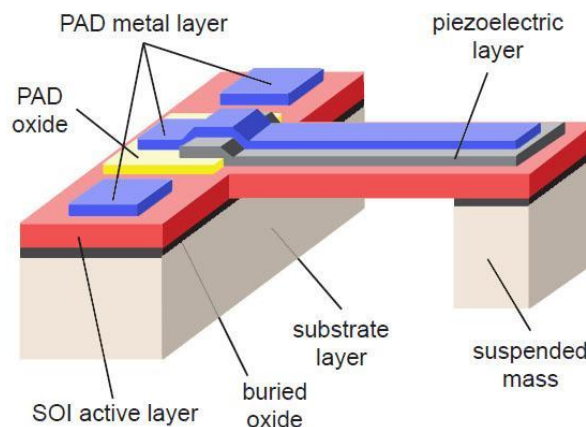


**Figure 3: Schematic of the MEMS different layers.**



PiezoMUMPS is a general-purpose low-temperature piezoelectric MEMS process. It was introduced by MEMSCAP in 2013 as an evolution from the well-known SOIMUMPS process that uses the same SOI wafers and also inherits some of its bulk and surface micromachining features. Additional advantages of this process are its reduced cost for research purposes and its high availability (three manufacturing runs scheduled per year).

The PiezoMUMPS process includes deposition and patterning of an Aluminium Nitride (AlN) piezoelectric film on top of a 10  $\mu\text{m}$  thick SOI device layer. The minimum feature size for the SOI layer is 2  $\mu\text{m}$ , making easy to obtain moveable structures with aspect ratios up to 5:1. For electrical connection and insulation purposes, the process also includes deposition and patterning of metal and silicon oxide layers.

## 2.3. Applications

### 2.3.1. LISA

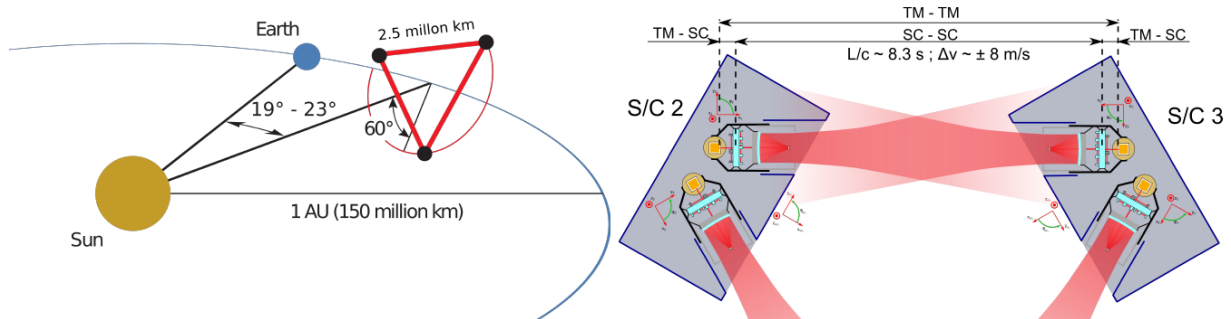


**Figure 4: Left: Lisa orbit. Right: Scheme of the LISA measurement principle.**

Laser Interferometer Space Antena is an ESA mission designed as a gravitational wave detector with high sensitivity in the mili-Hertz band. Three spacecrafts will host two free test masses each, and will be separated from each other 2.5 million kilometers, following a heliocentric orbit 20° behind the Earth. Each spacecraft is linked to the other by an infrared laser beam that allows the precise monitoring of the displacement between the test masses at each spacecraft. The cubic test masses act as end mirrors of the interferometer (Figure 4).

To detect gravitational waves, the test masses are in free fall on board the three spacecraft. The correct placement and free falling of the test masses is monitored by a set of capacitive sensors surrounding the free-floating test mass, and can act as a sensor or as an actuator, to apply micro-Newton corrections to the spacecraft by precision thrusters to keep them centered to their respective test masses.

The precursor mission LISA pathfinder, confirmed that the dominant magnetic contribution to the test mass, corresponds to the coupling fluctuations of the interplanetary magnetic field to the local gradient in the test mass position [4]. Hence, a magnetic diagnostic subsystem that is able to monitor those sub mili-Hertz magnetic fields is needed.

For those measures at LISA pathfinder a FluxGate sensor is used.

### 2.3.2. Planetary exploration

#### 2.3.2.1. MARS

MAG/ER investigation on Mars Global Surveyor (Flux Gate)

Solar wind interaction with Mars was studied by the Mars Global Surveyor (MGS). The Martian plasma environment changes in function of the solar EUV (extreme ultra violet) flux, upstream solar wind pressure and Interplanetary Magnetic Field direction [11]. Observations of magnetic oscillations in the range 5mHz to 0.1Hz are done as the ship crosses the different regions of the magnetosphere.

For those measurements a FluxGate is also used, as in LISA pathfinder.

MAG: Tri-axial fluxgate on board MAVEN

Magnetic field measurements on board MAVEN (Mars Atmosphere and Volatile Evolution) with a tri-axial FluxGate, allowed the detection of low frequency waves at Mars in the upstream region and in the magnetosphere, [12].

Flux Gate Magnetometer of InSight mission

Magnetic field fluctuations were measured on the surface of Mars by the InSight Flux Gate Magnetometer. This was able to detect static magnetic fields to detect remanent magnetization, and to improve the predictions of the surface magnetic fields obtained from MAVEN or MGS. Moreover, it is looking for low frequency time-varying fields allowing to understand diurnal variations. [13]

Another objective of the magnetometer is to quantify the magnetic interference on the Very Broad Band (VBB) seismometer. [14]

### 2.3.2.2. Others

Similar applications as the previously described can be seen in Mercury [15], Jupiter [16], Venus [5], Saturn-Titan-Icy satellites [17], [18], [19], the Moon [20], the Sun [21], and many others.

### 2.3.3. Low Earth Orbit

#### 2.3.3.1. LEO Satellites

The use of low noise and high-resolution magnetometers in LEO (Low-Earth Orbit) satellites can be divided in two main applications:

#### 2.3.3.2. Altitude and Orbit Control systems

In this application the magnetometer measures the earth magnetic field to provide the azimuth direction. Usually in small satellites an AMR (Anisotropic Magneto-Resistive) sensor, with a noise of  $< 16nT/\sqrt{Hz}$  at 1 Hz.

#### 2.3.3.3. Measuring Earths magnetism for geomagnetic and magnetospheric monitoring

The magnetic field changes with time and location and depends on the core magnetic field, the local anomalies in the lithosphere, underwater oceanic currents, ionosphere activity and magnetosphere and the interaction of the solar wind.

#### 2.3.4. Cold Atom interferometry

In atom interferometers, atoms of two different isotopes are sequentially captured, cooled, trapped and prepared in a high-vacuum vessel by orthogonal laser beams and magnetic fields. These atoms undergo a second stage of cooling in a magnetic trap on an atom chip. After loading into a dipole trap and further evaporation and cooling, the Bose-Einstein Condensate (BEC) state is reached. After successive interrogation with laser beams, the position of the atom clouds is then detected by light-influenced fluorescence using laser beams and photodiodes. Experiments with atom interferometers in space include the ACES/PHARAO experiment, to be operated in the ISS [22], in-orbit satellite Cold Atom Laboratory (CAL) [23], or experiments performed during sounding rocket flight [24].

Magnetic field monitoring and control is transversal to these experiments, given that the measurements have an intrinsic dependency with the magnetic field. The extreme precision needed by these experiments, set stringent requirements on the sensitivity of the sensors, and, if the sensor needs to be close to the BEC, it will require a minimum magnetic impact in the experiment and a minimum power dissipation.

### 3. TMR

The device used is the single-resistor bare die TMR9001 from Multidimension (Fig. 5). The sensor is needed to be in a bare-die form since we want the MEMS cantilever tip to come as close to the sensing area as possible, which will allow us to obtain a better modulation efficiency.

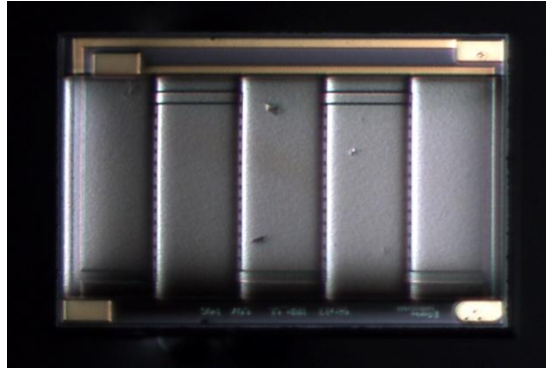


Figure 5: Image of the TMR9001 bare die.

This device has a nominal resistance of 50 k $\Omega$ , and a measurement range of +/- 400  $\mu$ T. The magnetic noise density spectrum shows a clear 1/f noise, with 0.4 nT/ $\sqrt{\text{Hz}}$  @1 Hz. Although this last measurement was done with a full-bridge with four sensors, and it is obtained from the datasheet.

In our application, it was decided to have a single sensor and three fixed resistances, in a Wheatstone bridge configuration. For this case, the sensitivity is four times lower, of  $\alpha=0.4$  mV/V/ $\mu$ T, when for the full system (with four TMR in a full bridge configuration), the sensibility is  $\alpha=1.6$  mV/V/ $\mu$ T, being the Resistance of system:

$$R = R_0(1 + \alpha B) \quad (1)$$

#### 3.1. TMR Characterization

To verify that the device noise floor is compliant with the specification, the TMR is mounted inside a mu-metal chamber (see chapter 5), consisting of three concentric cylinders of mu-metal, a high magnetic permeability material which shields the components inside of it from the external magnetic field (Fig. 6). The device is attached to a 3D-printed structure to place it in the center of the chamber.

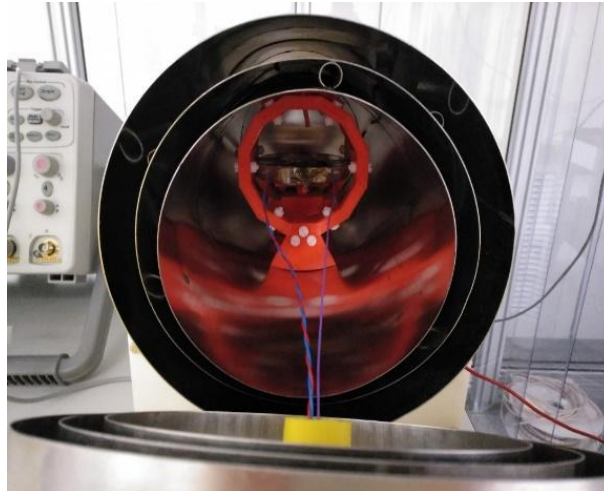


**Figure 6: Set-up for the sensor noise characterization.**

The bridge was biased with 1 Vdc level, hence, the theoretically expected sensitivity should be  $400V/T$ . A noise measurement was performed with an acquisition system previously used for the ESA LETS project at the Institut Català del Espai, and it can be observed in Fig. 7. The measured data is labelled as “channel\_9”, the noise given by the datasheet with a bias of 1 V is shown in green. The noise of the datasheet matches the measured noise, but scaled up by a factor close to 4.

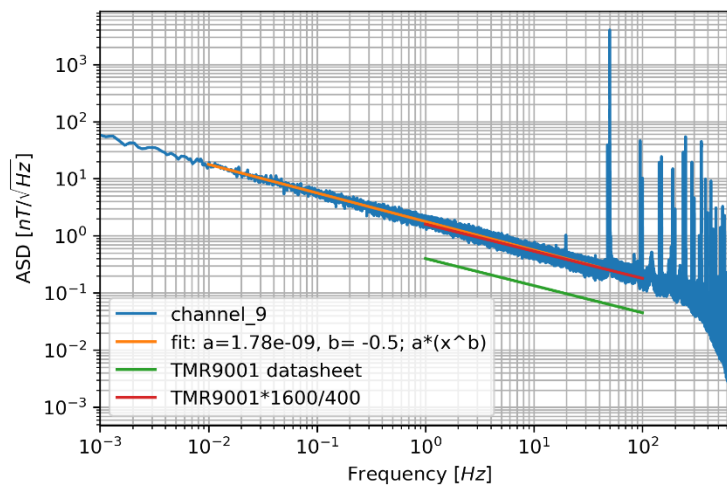


**Figure 7: Noise floor measurement of the sensor.**

The noise has been fitted in the low frequency range, and the obtained value of it is:

$$S_B^{1/2} = 1.778 f^{-0.499} nT/Hz \quad (2)$$

With this equation, we get  $0.4 nT/\sqrt{Hz}$  at 210 Hz, and  $176 nT/\sqrt{Hz}$  at 0.1 mHz. Note that in Fig.7 the minimum frequency is 1 mHz, at 0.1 mHz the noise will be higher. Therefore, the noise is well above the  $10 nT/\sqrt{Hz}$  at 0.1 mHz, which is the maximum objective noise for this work.

#### 4. MEMS used

In accordance with the sensor design constraints, three MEMS resonator models were designed and manufactured, all in the form of a 4 mm length SOI+AlN+metal cantilever. The 5-mask layout of a die is reproduced in Fig. 8, showing the geometrical arrangement of the three resonator models. Additionally, a 3D view of the models is shown in Fig. 9.

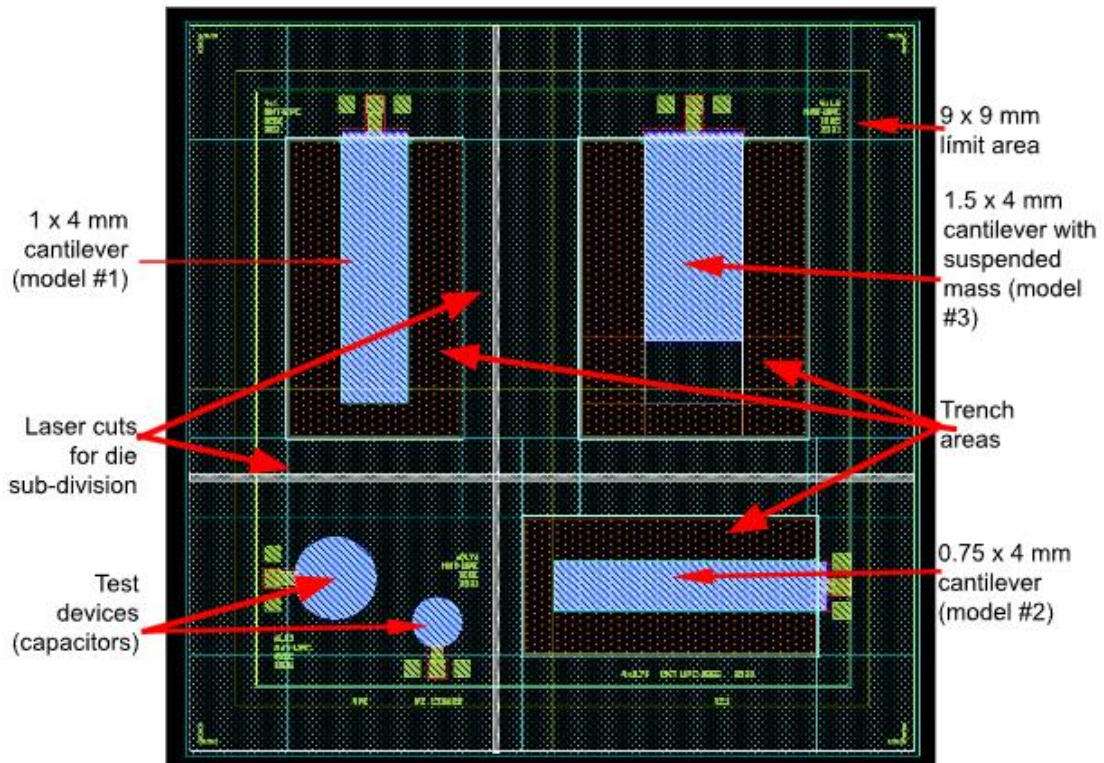


**Figure 8: Layout of the PiezoMUMPS resonators fabricated.**

As can be seen in Figure 8, models #1 and #2 differ only in the width of the cantilever (1 mm and 0.75 mm respectively), while model #3, which is 1.5 mm wide, and has a mass suspended at its free end. The purpose of this mass is to drastically reduce the frequency of the first mechanical mode of oscillation. Note that all devices have 3 PADs: a central one for voltage actuation (connected to the metal layer) and two lateral ones for ground (both connected to the SOI active layer).

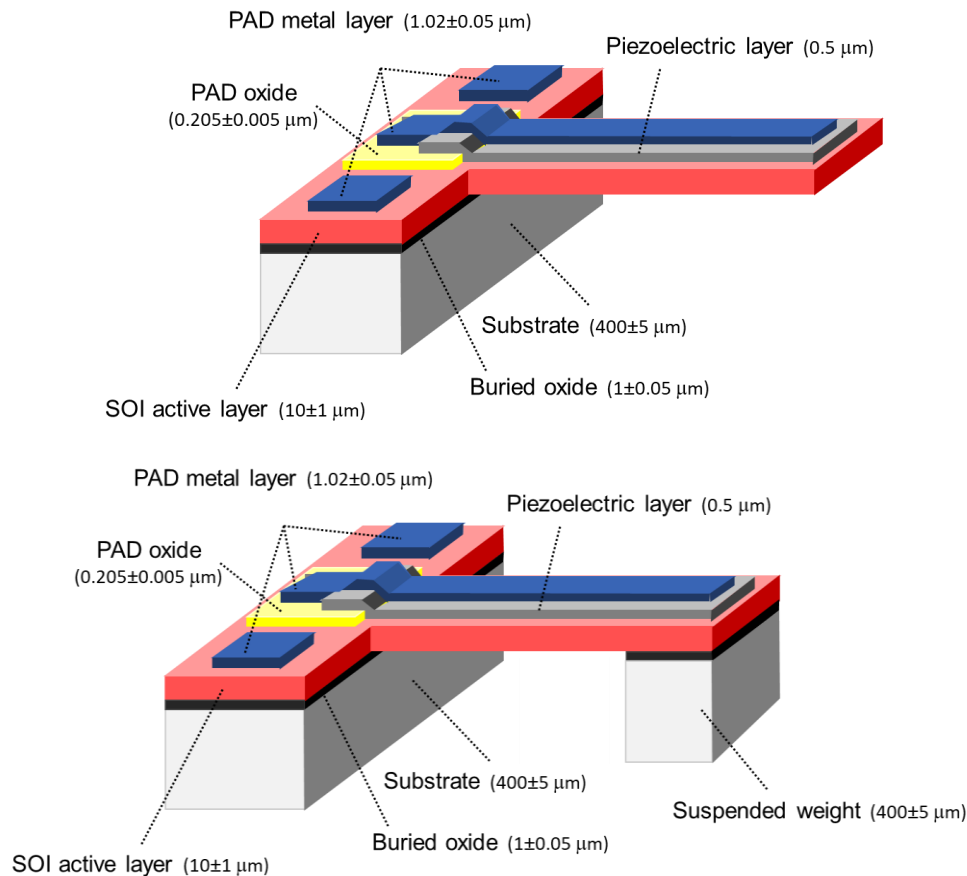


**Figure 9: 3D schematic of the PiezoMUMPS resonator models fabricated. Top: simple cantilever shape, with two sizes: model #1 (1 x 4 mm) and model #2 (0.75 x 4 mm). Bottom: model #3: cantilever with suspended mass of size 1.5 x 4 mm; mass size is 1.5 x 1 x 400 μm**

Comsol FEM simulations were performed to estimate the mechanical frequency response of the MEMS devices designed. As an example, the results obtained when applying a 1V AC actuation to models #1 and #3 are reported in Fig. 10. It is seen there that the first mechanical resonance for model #1 is expected to be at 925-950 Hz, whereas, as expected, this value decreases to 190-195 Hz for model #3. It is also shown that a good quality factor (i.e. that typical of low pressure conditions) is of key importance to achieve the range of amplitude displacements needed for the sensor.

Finally, Fig. 11 shows a picture of a manufactured die, before and after device individualization. The manufacturer delivers 15 dice in each manufacturing batch. Thus, in our case we theoretically had 15 copies of each resonator model. However, it should be noted here that, due to a specific problem that occurred in our manufacturing batch (later recognized by the manufacturer), some devices were damaged. Specifically, they showed insulation leaks in the thermal oxide, which reduced dramatically its impedance between terminals. Due to this unpredictable reliability issue, the number of devices we have been able to use is lower than 15. Furthermore, some of the usable devices show brittleness with voltage stress, making it necessary to apply low voltages to preserve their durability.

Another observed effect (this one already foreseen beforehand and then taken into account in the positioning and alignment of the system components) is the bending due to the residual stress that typically occurs in large MEMS cantilevers such as those designed.

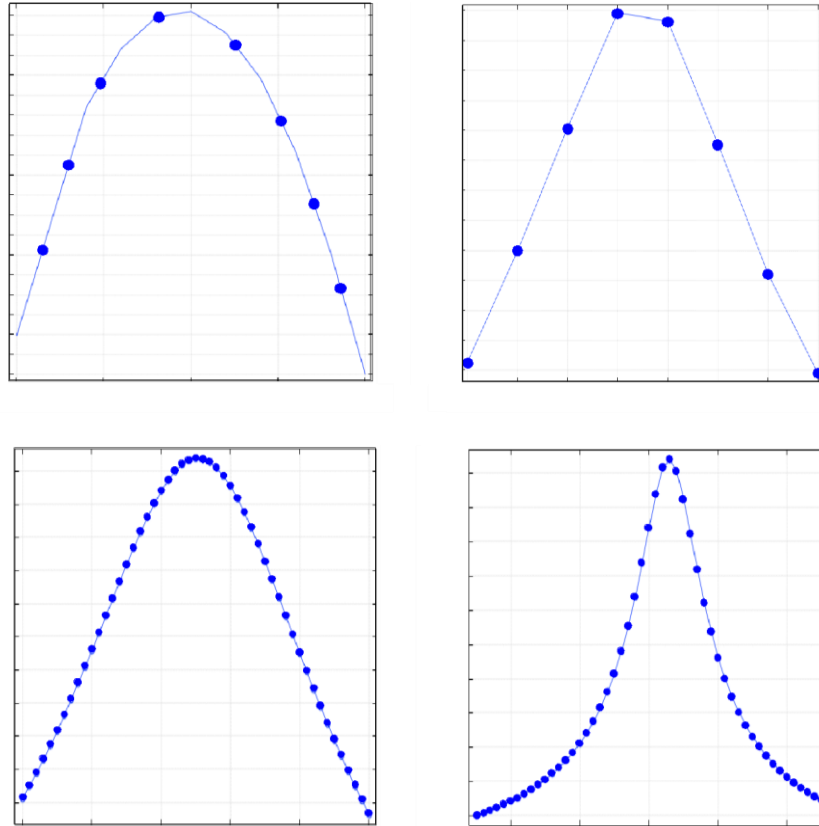


**Figure 10: Results obtained from COMSOL FEM simulations of the MEMS cantilevers. The graphs show the displacement amplitude around the first mechanical resonant frequency obtained applying 1V AC to the device. Top graphs correspond to device #1 (simple cantilever) and bottom graphs correspond to device #3 (cantilever with suspended mass), each for two quality factors.**

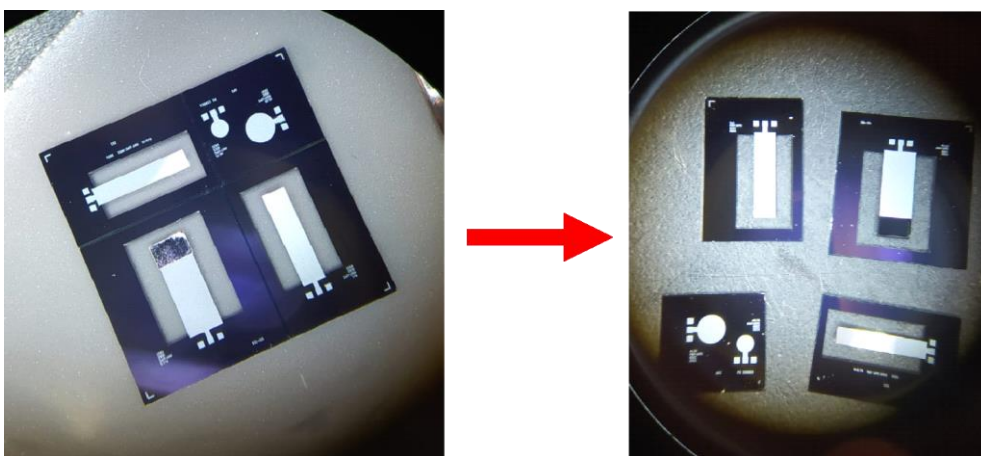


**Figure 11: Manufactured die and device individualization.**

After separating the dies (Fig 11), a piece of mu foil tape of 1.5 mm x 1 mm (the same dimensions as the TMR) is attached on the cantilever surface to modulate the magnetic

field in the surface of the sensor once it is positioned, then the MEMS is mounted to a PCB using epoxy, and wire-bondings are done, see Fig. 12.



**Figure 12: MEMS cantilever with mu foil tape attached.**

### 4.1. MEMS Characterization

In order to characterize the MEMS resonators, the conductance and the susceptance of the devices is measured with a HIOKI chemical impedance analyzer by exciting the MEMS at different frequencies, to determine the resonant frequency (where the conductance is maximum). This instrument has been used instead of a classical impedance analyzer due to its higher precision, especially in the low-frequency ranges.

Figure 13 shows the circuitual model used to analyze the MEMS response, taken from [25]. It includes the lumped electro-mechanical model of the MEMS resonator, which consists of an inductance (cantilever mass), a capacitance (spring/cantilever recovery force), and a resistor (damping losses) in series. Additionally, a parallel resistor and a parallel capacitor are used to model the electrical parasitic effects of the system, as the resistance and capacitance between the actuation electrodes.

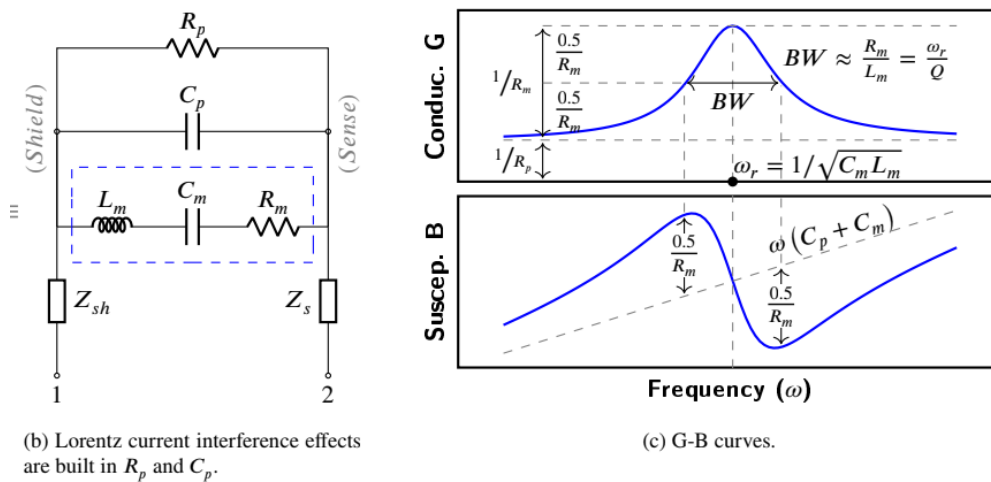


Figure 13: Model for the impedance response of the MEMS cantilever, from [25].

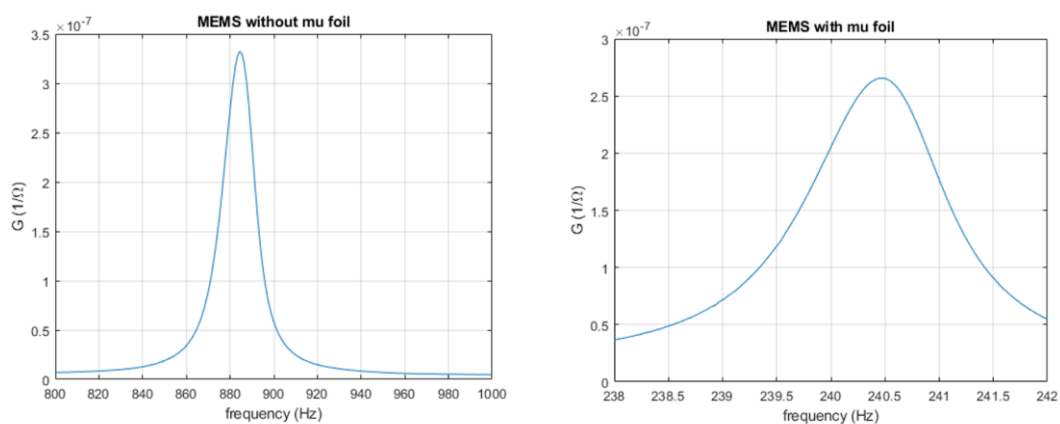


Figure 14: Comparison of the impedance response of a MEMS cantilever with and without mu foil.

It is important to note that the resonant frequency of the cantilever shifts to lower values after the mu foil layer is attached. For instance, with the 1 mm width MEMS the frequency

reduces from ~800-900 Hz down to ~200-250Hz, see Fig. 14. This is an expected result, since the cantilever mass is increased and the resonance frequency ( $f_r$ ) is proportional to  $1/m$ , being  $m$  the mass.

It should be noted here that due to a specific problem that occurred in our manufacturing batch (later recognized by the manufacturer) some devices were damaged. Specifically, they showed leaks in the thermal oxide, which reduced dramatically its impedance between terminals and made some devices not usable. Furthermore, some of the usable devices show brittleness with voltage stress, making it necessary to apply low voltages to preserve their durability.

Applying high voltages to obtain high displacements of the cantilever was not an option, due to the brittleness of the MEMS against voltage stress. Then, to obtain high displacements applying small voltages measurements were done with the MEMS working at low pressure, placed inside a vacuum chamber (Fig. 15).



**Figure 15: Vacuum chamber.**

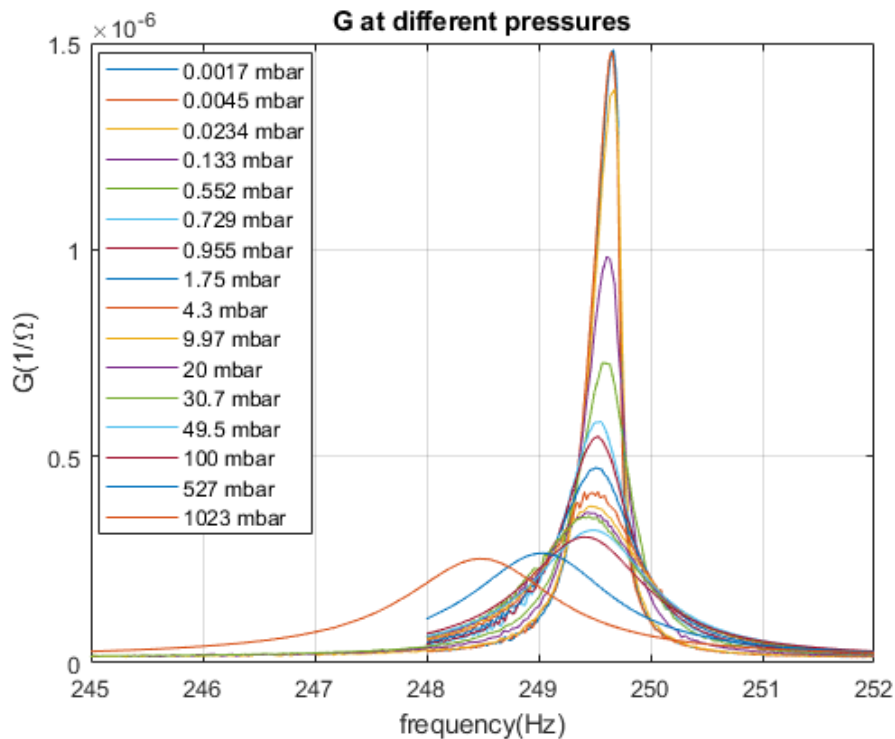


**Figure 16: Impedance response of a MEMS cantilever with mu foil at different pressures, with a constant actuation amplitude.**

Several measurements were performed to study the behavior of the MEMS in low pressure conditions. For example, Fig. 16 shows the spectra of the conductance obtained under different pressure values, with a constant actuation amplitude. As it can be seen, decreasing the pressure not only makes the conductance (or displacement) to increase, but it also shifts the resonance frequency of the cantilever. This result agrees with general MEMS theory, which indicates that by reducing the pressure (thus, the damping losses), both the quality factor and the resonant frequency tend to increase.

Another typical result is that the improvements due to working at low pressure conditions become quasi-saturated below a given pressure level. In other words, at a certain pressure level is not worth further reducing the pressure because very little is gained.

Then, an experimental study was done to determine the optimal pressure range to use, such that small pressure variations would not affect significantly the resonant frequency or the displacement. The results obtained are shown in Fig. 17, where the evolution of both the resonant frequency and the maximum conductance for low pressures are plotted. As it can be seen there, displacement is the limiting figure in our case, and makes it advisable to work with pressures of 0.01 mbar or less.

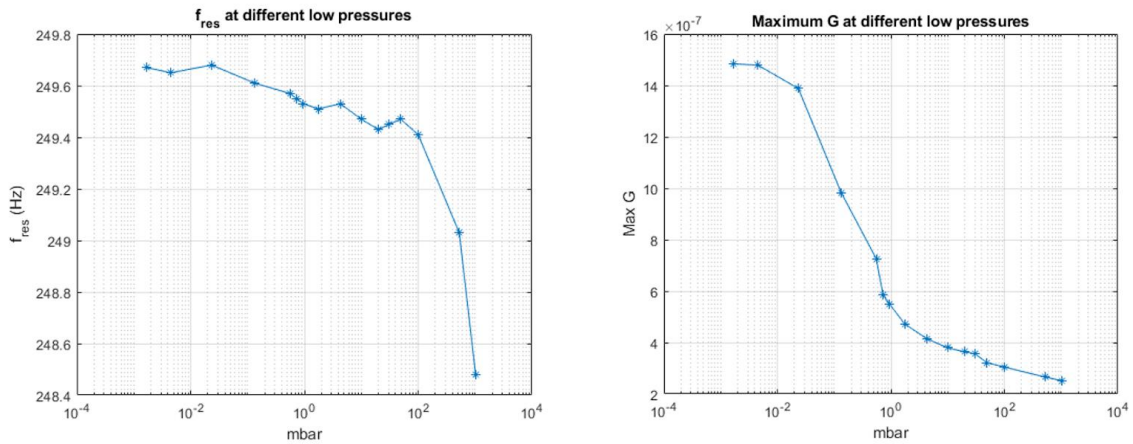


**Figure 17: Evolution with pressure of the resonant frequency and the maximum conductance.**

We also investigated the evolution of the quality factor of the resonator with pressure. To this effect, fittings of the experimental data with the following model for the electrical admittance the MEMS, taken from [25], have been performed:

$$G(\omega) = \frac{1}{R_p} + \frac{R_m}{R_m^2 + \left(\omega L_m - \frac{1}{\omega C_m}\right)^2} \quad (3)$$

$$B(\omega) = \omega C_p - \frac{\omega L_m - \frac{1}{\omega C_m}}{R_m^2 + \left(\omega L_m - \frac{1}{\omega C_m}\right)^2} \quad (4)$$

Being the quality factor:

$$Q = \frac{1}{R_m} \sqrt{\frac{L_m}{C_m}} \quad (5)$$

Figure 18 shows the evolution with pressure of two circuital parameters,  $R_m$  (directly related to damping losses) and the quality factor ( $Q$ ). As it can be observed,  $R_m$  monotonically decreases with pressure (as the damping losses). As expected, this evolution is directly related to the one of the maximum conductance shown in Fig. 17.

On the other hand, and also as expected, the quality factor  $Q$  increases considerably when reducing pressure. Note that values above 800 are achieved for the chosen working pressures of 0.01 mbar or less.

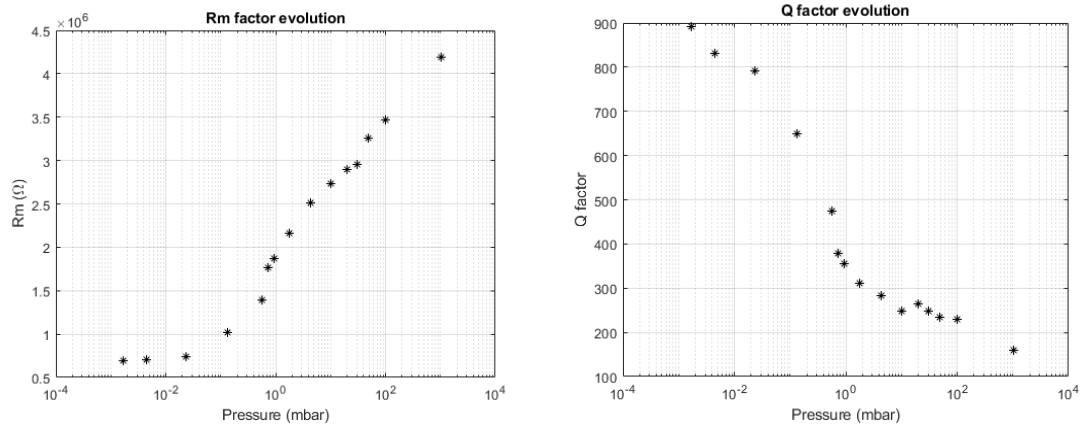


Figure 18: Evolution with pressure of the damping losses (Rm) and the quality (Q) factors.

## 5. Project development

### 5.1. Setup Components

#### 5.1.1. Mu-metal chamber

Mu-metal is a nickel-iron ferromagnetic alloy with a very high magnetic permeability. In this work, a 3-layer mu-metal chamber (Fig. 19) is used in order to shield the sensor from the external magnetic field and be able to measure the intrinsic sensor's noise.

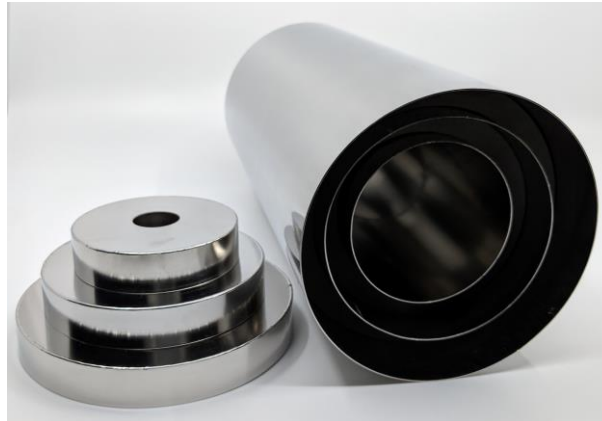


Figure 19: 3-layer mu-metal chamber.

#### 5.1.2. Helmholtz Coils

Device used to produce a region of nearly uniform magnetic field. It consists of two coils on the same axis and in the same direction, and spaced between them, the length of their own radius. See fig. 20.

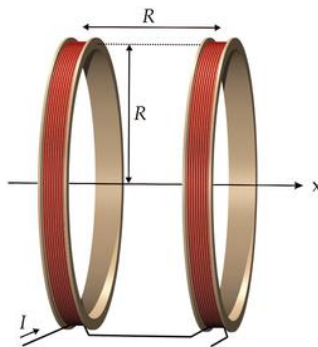


Figure 20: Helmholtz coil schematic.

The ones used in this work (Fig. 21), are used in order to obtain the modulation depth of the systems (see chapter 7.1), and to obtain the sensitivity of the sensor (as a known magnetic field can be produced). Also, Helmholtz coils were developed (Fig. 22) specifically for this work in order to be able to fit it inside the mu-metal chamber with the sensor mounted in it.



Figure 21: Commercial Helmholtz coil used



Figure 22: Helmholtz coils developed to fit inside the mu-metal chamber.

### 5.1.3. Temperature and Humidity controlled chamber

A device from the Institut Català del Espai (ICE), capable of controlling temperature with a  $\pm 0.1^\circ\text{C}$  of error, and Humidity with a  $\pm 0.1\%$  RH (Fig. 23). Which is used in order to measure the sensor's intrinsic noise (without taking into account possible deviations due to temperature).



Figure 23: Temperature and Humidity controlled chamber

## 5.2. Alignment and mounting the system

### 5.2.1. Magnetic Flux Concentrators

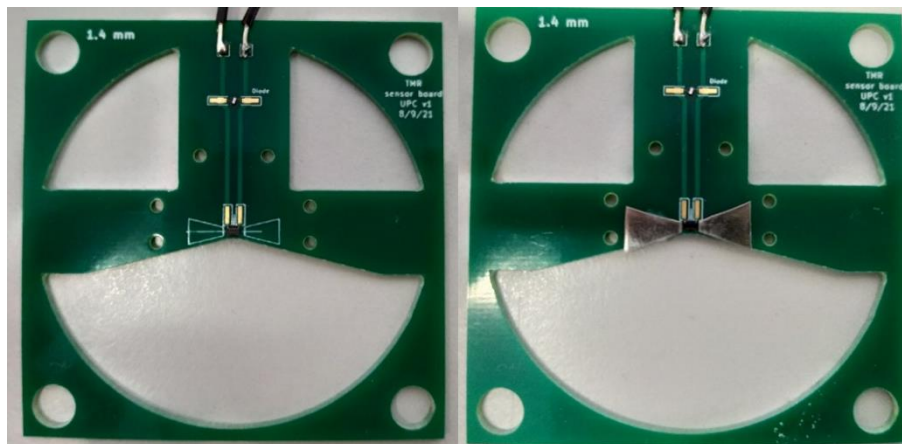


Figure 24: PCB with the TMR only (left), and after attaching the MFCs (right).

The TMR sensor is attached to a PCB through an epoxy and the required wirebondings are used for its electrical connection to the board. Afterwards, the magnetic flux concentrators are cut from a commercial 150um thick sheet of mu-metal, and they are added to the PCB using a commercial epoxy as shown in Fig. 24.

### 5.2.2. High mu-material on MEMS

Accurately and efficiently depositing a thick mu-metal layer on the free end of a MEMS cantilever is a complicated task, aggravated by the fact that the device is mechanically very fragile.

Preliminary mu-metal deposition tests were performed in the UPC clean room, using sputtering and evaporation processes Figure 25. But no deposition of mu-metal was accomplished with sputtering, and with evaporation only a layer of 160 nm was accomplished, which is not enough to have any modulation, since the project needs at least a 15  $\mu\text{m}$  thick layer.



Figure 25: Sputtering (left) and evaporation (right) chambers

Therefore, for prototyping purposes, it was decided to deposit the mu-metal to the cantilever using commercial 3305 tape from INFRATON, which consists of a 23  $\mu\text{m}$  thick layer of mu-metal with a standard adhesive layer. The tape was mechanically cut into 1 x 1.5 mm pieces. Afterwards, each piece was deposited manually on the tip of the MEMS cantilever. An example can be seen in Fig 26. It is important to note that, due to the augment of mass of the cantilever, the resonant frequency of the MEMS cantilever decreases from  $\sim 800\text{-}900$  Hz down to  $\sim 200\text{-}250$  Hz.

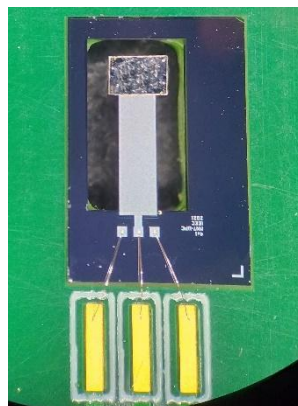
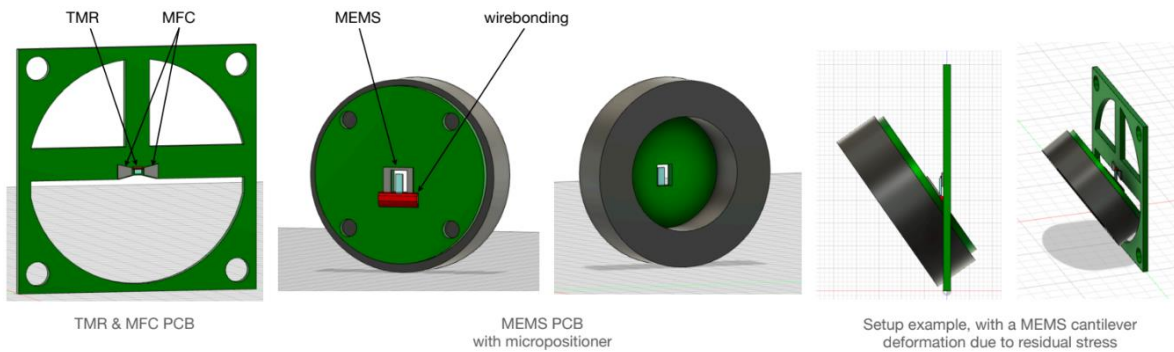


Figure 26: MEMS device in a PCB, with the wire-bonding and the mu-foil deposited.

### 5.2.3. System assembly and positioning

One of the key procedures of the project is correctly aligning the TMR and the MEMS cantilever. To optimally achieve this precise alignment is essential, in order to obtain qualitative results of modulation efficiency, hence a good sensitivity, and therefore, a low noise floor.



**Figure 27: 3D schema of the assembly/positioning of the MEMS PCB and the TMR PCB.**

The method used to align the system is described in fig 27. Where two PCBs (the MEMS PCB and the TMR PCB) are designed to achieve a wide angle adjustment range, to allow it to override the residual stress bending of the cantilever due to its fabrication.

To start mounting the system, the MEMS PCB is bolted to a Thorlabs K6XS micro positioner (FIG 28 a), which allows small positioning adjustments in X, Y, Z, yaw, pitch and roll axes. Also, a structure has been made with 3D printing (Fig 28. b), which provides support for the TMR PCB and the micropositioner with the MEMS.

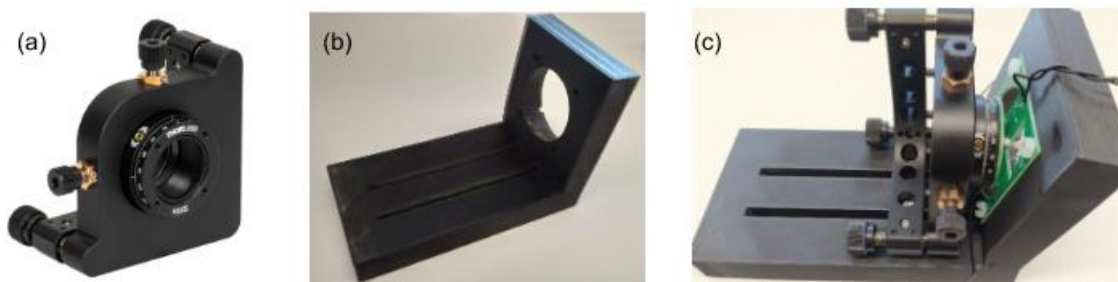


**Figure 28: Micropositioner used to fix the MEMS PCB board (a). 3D printed part to fix the TMR PB board and the micropositioner (b). Full alignment system mounted, with the 3D printed part, the micropositioner and both PCBs mounted (c).**

The procedure to correctly align the MEMS cantilever with the TMR is the following:

- A frequency sweep is applied to detect the maximum conductance of the MEMS (which is where the displacement of the MEMS is maximum) [25], and corresponds to the resonance frequency of the cantilever, see fig. 29 a. This measure is done in low pressure conditions ( $10 \mu\text{bar}$  range), using a vacuum chamber, see fig. 29 b, allowing it for greater displacement, due to less damping, for low voltages (as high voltages could eventually damage the devices).

- A Helmholtz coil (Fig 29 c) is used to create a known and oscillating magnetic field. The sensor structure is placed inside the vacuum and inside the Helmholtz coils. Then, without the MEMS, the magnetic signal generated by the Helmholtz is recorded. Then, the MEMS PCB is installed and positioned, afterwards, another measurement of the sensed magnetic field is achieved while exciting the MEMS at its resonance frequency, and therefore the system is modulating the magnetic field.

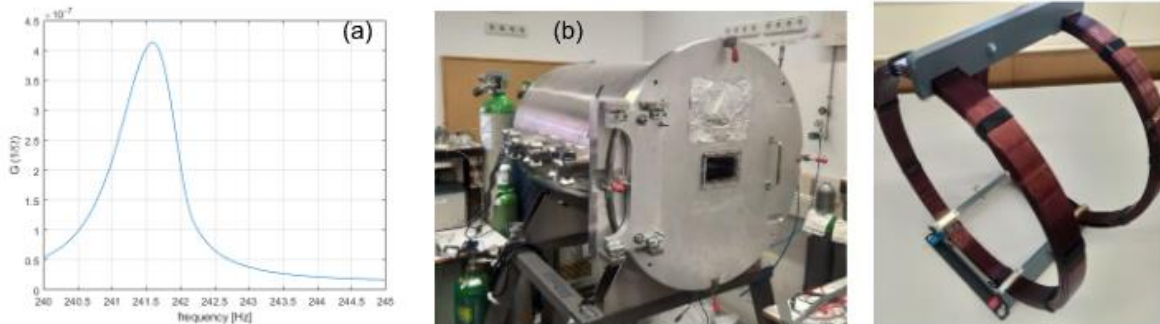


**Figure 29: Frequency swept of the conductance used to detect the resonance frequency (a). Vacuum chamber used at UPC (b). Helmholtz coils used to create a homogeneous and controlled magnetic field (c).**

With the previously obtained measurements, the modulation efficiency can be calculated as:

$$\text{Modulation Depth} = e = 2 \frac{B_x}{B_{nf}} \quad (6)$$

Being  $B_{nf}$  the amplitude of the magnetic field created by the Helmholtz Coil when sensed without the cantilever, and  $B_x$  the amplitude of the modulated signal, once the cantilever is installed and excited at its resonance frequency.

To obtain a good sensitivity it is important to have a high modulation efficiency, so if the result of the modulation efficiency obtained is poor, the position of the MEMS is modified using the micrometric bolts of the micropositioner, and the measurement is repeated. This procedure is iterated until the modulation depth factor is optimized (see chapter 7.1).

- Eventually, once the system is successfully positioned, both PCBs are attached to each other, conserving their respective position. This is acquired by using 1 mm diameter quartz rods driven through holes in both PCBs, see Fig 30. And the rods are bonded to the boards using epoxy, see Fig. 31. The bonding is done in the UPC clean room, Fig. 31, where the undesired effects as pollution or daily temperature cycling are reduced. The epoxy used is the 302-3M, from Epo-tek, which cures at room temperature. The use of other epoxies was avoided, because they need to cure at high temperatures, and misalignment happened due to the different expansion coefficient of the components, therefore high modulation efficiency was lost.

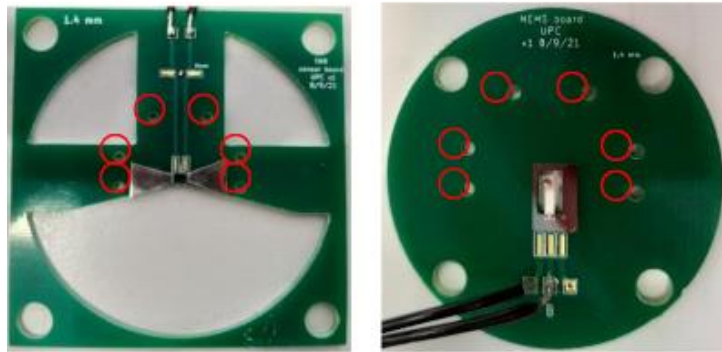


Figure 30: Both PCBs TMR + Magnetic Flux concentrators (left) and MEMS (right). Note that the holes for the future fixation of the system are circled in red.

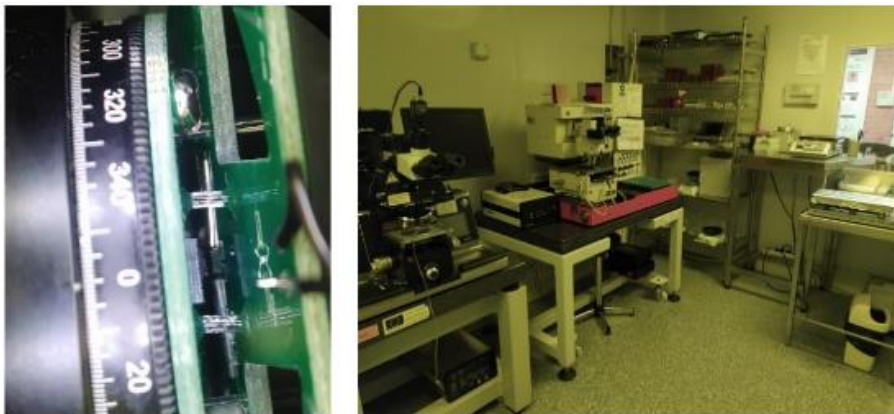


Figure 31: (Left) picture taken with microscope of the glass rods and epoxy used to fixate the systems. (Right) UPC clean room where the system is mounted.

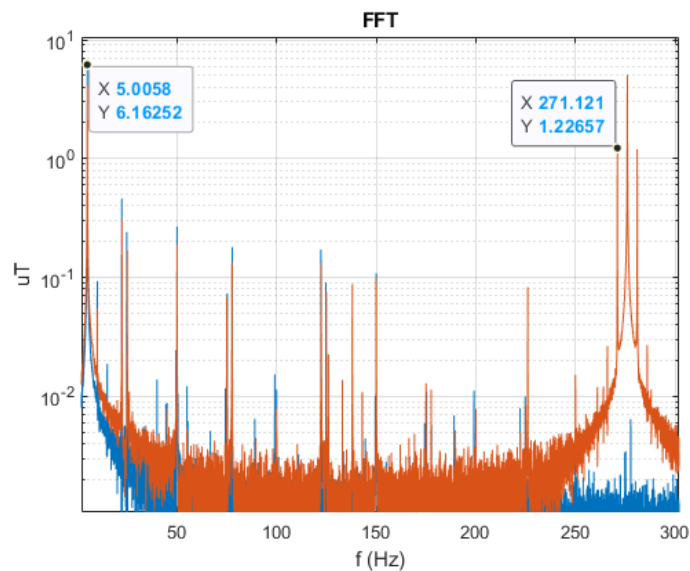


Figure 32: Fast Fourier Transform of both signals, without MEMS (blue) and with MEMS modulating the signal (orange). Measurement used to obtain the modulation depth.

Figure 32 shows an example of the experimental results obtained of modulation efficiency, where a 39% was achieved (more information about the modulation can be found in depth in chapter 7.1).

## 6. Characterization electronic system

An electronic front-end system was developed especially targeting the developed sensor, the requirements for the electronics are:

- Low noise: the electronic noise must be below  $10 \text{ nT}/\sqrt{\text{Hz}}$ , so it is below the interplanetary magnetic fields.
- The system needs to sample the modulated signal and the excitation signal in sync, to be able to demodulate the signal once it is received.
- The excitation signal of the MEMS must also be generated by the electronics, and at the same time, it must be in sync with the acquisition.
- Sampling each signal with  $100 \text{ KS/s}$  (the excitation and the modulated) is required in order to avoid aliasing and to have room for future MEMS cantilevers with higher resonance frequencies.

In order to achieve these specifications, an electronic circuit was developed specifically for this purpose (Fig. 33 and 34). It consists of:

- A TMR acquisition system, formed by a Wheatstone bridge and a differential instrumentation amplifier structure to amplify the signal, an anti-aliasing filter, and an ADS8318 ADC to sample the sample at a  $100 \text{ kHz}$ .
- A MEMS excitation signal, that consists of a DAC8831ICD digital to analog converter, to create the excitation signal, an anti-aliasing filter, the same filter used in the TMR, so both channels are in phase, and ADS8318 ADC to sample the signal.
- To be able to read the data from the ADCs and to create the excitation signal in the DAC, a digital board NUCLEO f401re was used.
- And to broadcast the read signal to a computer to store and process the data an FTDI board (SPI - USB) was used.

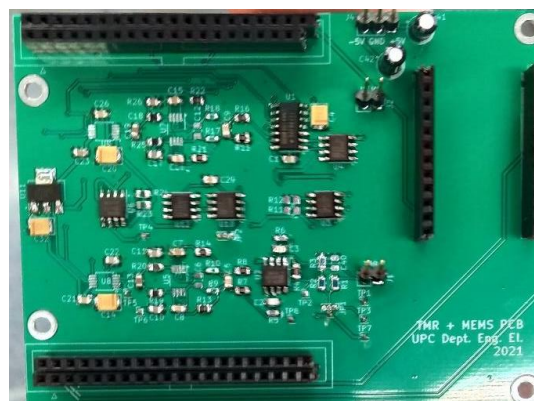


**Figure 33: Developed analog board for the excitation of the MEMS and the acquisition of the signals.**

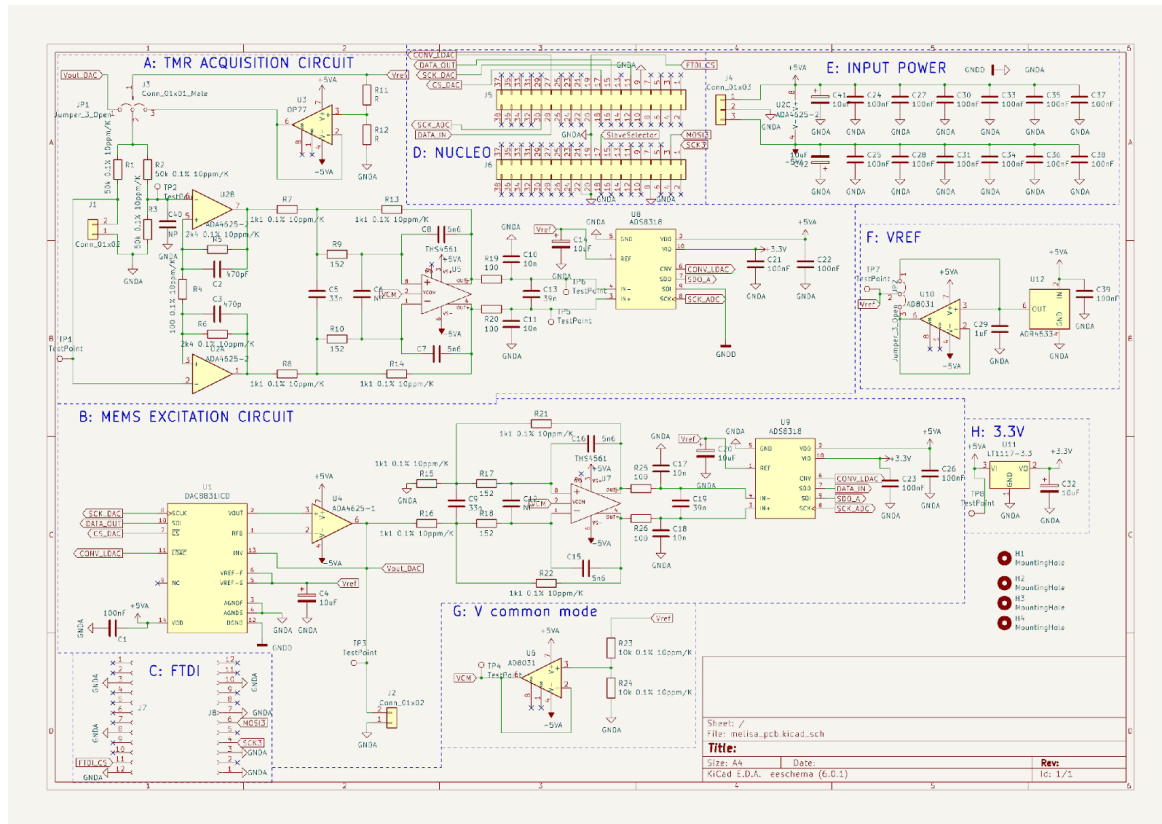


Figure 34: Analog board schematic.

After capturing the sensor data, a synchronous demodulation recovers the low frequency contents of the magnetic field that was present near the sensor.

The extreme low frequency of the field measuring makes the digital processing an ideal solution. What is more, the timing requirements of the systems makes microcontroller-based system suitable to the task. To that end, a system built around an STM32F401 microcontroller that features and ARM Cortex M4 CPU has been developed.

To minimize the noise in the acquisition, we use external ADCs and a DAC. Meaning that the MCU deals only with digital data, therefore an optimized for real-time digital I/O MCU has been selected.

As per previous explanation the system has one sensor, the tunneling magnetoresistance (TMR), and one actuator: the magnetic field modulator MEMS system. In order to interface with those elements, two ADCs and one DAC have been included on the system. The DAC will provide the excitation of the MEMS resonator. As we want to know the exact modulation phase applied to the magnetic field to properly carry out the demodulation, an ADC has also been included to measure the final excitation applied to the resonator after the conditioning circuits.

The second ADC is devoted to the measurement of the TMR signal output.

The selected ADCs and the DAC communicate with the CPU using SPI buses. One SPI bus is used for the two ADCs that are daisy chain connected and a second SPI bus is devoted to the DAC. The use of two independent SPI buses enables to parallel use them so the data bandwidth is increased.

The MCU works at a constant sample rate in the DAC and both ADCs. The MEMS is driven by a sine wave generated by the DAC that is updated at each sample point and both ADCs are read also at each sample point.

The sinewave DAC data is generated in real time using ARM optimized 32-bit trigonometric function code.

The data read by the ADCs is then sent to a PC connected to the MCU.

The microcontroller is connected to the PC using three independent interfaces inside two USB hardware connection.

The first and second interfaces are integrated in a single USB hardware connection.

The first interface is the debug SWD connection. This interface enables ISP programming of the MCU and enables the hardware debugging of its operation.

The second interface is a serial over USB COM connection. This connection provides information about the operation of the MCU and user interaction using a serial terminal.

Finally, the third interface, that uses a dedicated USB hardware connection, provides the ADC data to the PC. To provide this data, the data is sent from the MCU to a FTDI SPI/USB bridge that relays the data to the PC using a custom USB endpoint.

All the described digital operation of the system is summarized in Fig. 35.

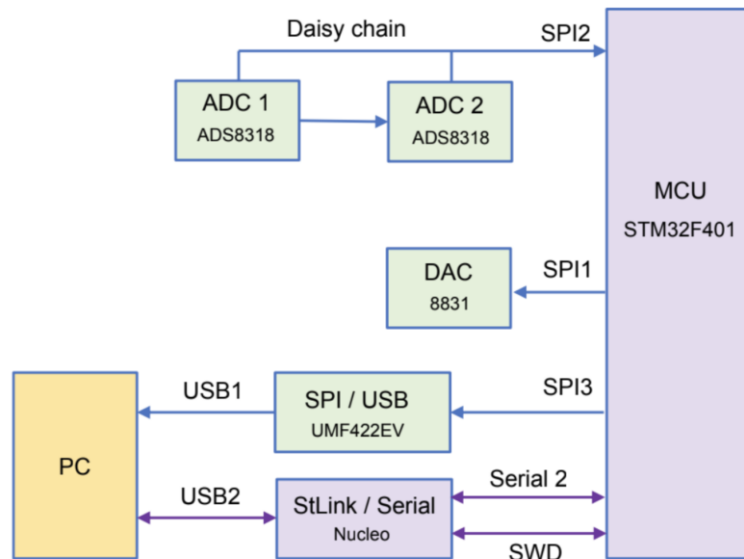


**Figure 35: Digital operation of the system.**

The software of the system is distributed between the PC and the microcontroller.

The Pc hosts the high-speed SPI to USB bridge driver, the FTDI library that interfaces with the driver and the code that implements the final application on the PC side.

This application configures the bridge on start-up, gets the RAW ADC data, performs synchronization, frame error detections/corrections, demodulates the data, filters it and records it in a document.

In order to provide low-jitter and real-time operation of the system, the operation of the MCU firmware operates around a hardware timer synchronization signal.

A CONVST/LDAC signal is generated by a MCU hardware time and feed to the DAC and the ADCS. On the rising edge of the signal the ADC data is captured and, on the falling edge, the DAC is updated. As the MCU clock is generated by a quartz oscillator and due to the use of ha hardware timer sample signal we obtain the minimum jitter in the ADC and DAC operation.

The firmware syncs with this hardware signal to carry out all its actions. It is important to note that, as long as the firmware is capable to sustain the computing and communication load, the system will work as intended as the source of potential jitter errors has been solved by hardware.

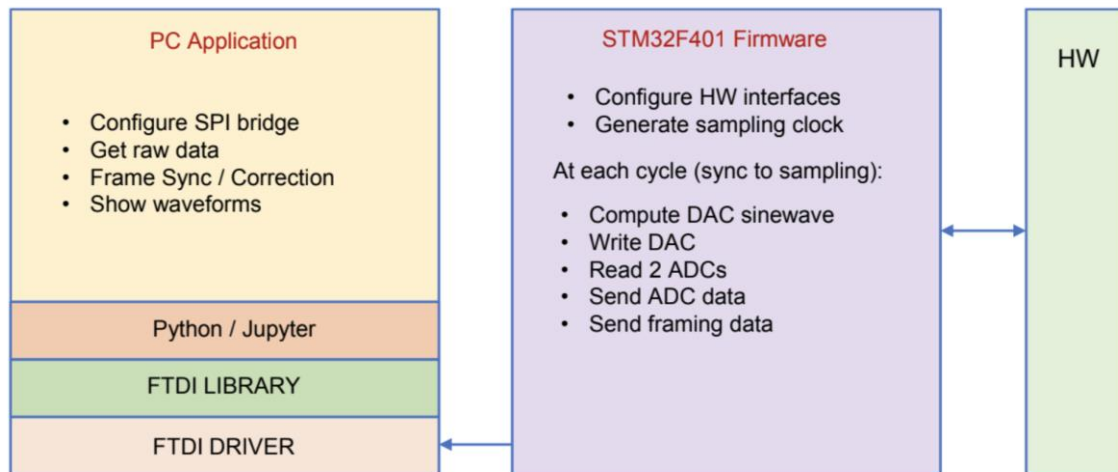


**Figure 36: Diagram of needed functions for the PC application and for the STM23F401 Firmware.**

As previously explained, sinewave DAC data is generated by ARM optimized 32-bit code. This calculation code is executed during the time it takes for the ADCs to perform the conversions.

After the conversion of both ADCs, the data from the ADCs is read at the same time that the data is provided to the DAC and the PC.

On each sample interval, the ADC data of this interval is read, the DAC data is fed before the update edge and the ADC data from the previous sample interval is sent to the PC.

Frame information is also added also when sending data to the PC to detect undesired data packages loss in the FTDI bridge.

Figure 37 shows the timing diagram of all those operations for a sampling frequency of 100 kHz.

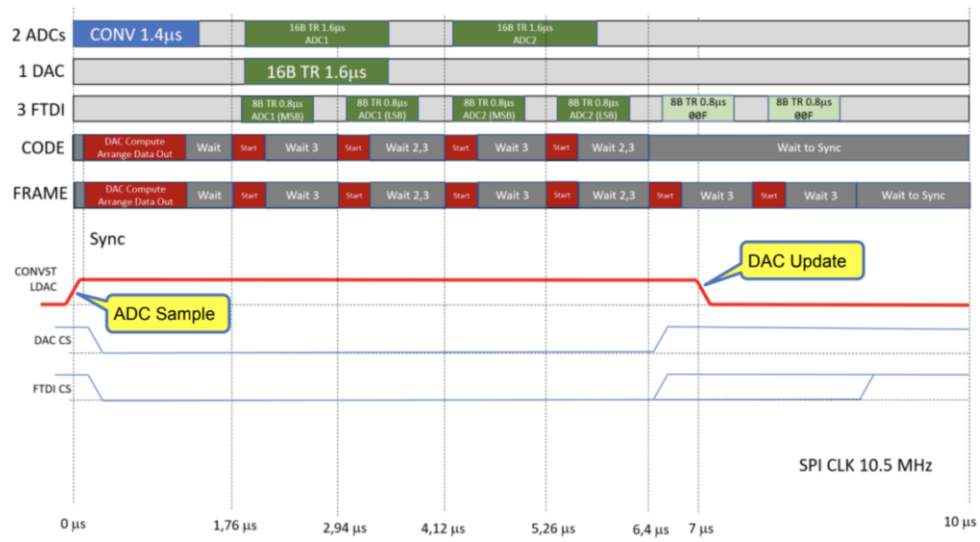


Figure 37: Timing diagram of the system.

## 7. Results

### 7.1. Modulation Depth

Modulation depth has been used throughout the project as figure of merit to check the quality of the modulation, the quality of the positioning of the TMR and MEMS cantilever couple and therefore to ensure a high system sensibility. It is defined as the ratio between the original magnetic field signal and the modulated one, times two, so the theoretical maximum modulation depth will be 100%.

$$e = 2 \frac{B_x}{B_{nf}}$$

Being  $B_{nf}$  the amplitude of the original magnetic field (without the MEMS cantilever) usually created using Helmholtz Coils, and  $B_x$  the amplitude of the modulated signal once the cantilever is installed and excited at its resonance frequency.

To achieve this measurement, first of all, the resonance of the cantilever is detected with a precision impedance analyzer. A frequency sweep is applied to detect the conductance maximum, which corresponds to the resonance frequency of the MEMS (where the MEMS displacement is also maximum), see Fig. 38 a. This measurement is done in low pressure conditions, using the vacuum chamber at the UPC facilities, see Fig. 39. Apart from reproducing more realistic working conditions for the sensor (in the vacuum of space), this vacuum improves the quality factor of the MEMS, allowing greater displacements without having to apply high voltages that could eventually damage the devices.

The next steps involve using a structure with Helmholtz coils to create a known-value and oscillating magnetic field, see Fig. 38 b. The structure is placed inside the vacuum chamber and a set of low-pressure measurements is done. Once we have a known and controlled magnetic field in the center of the coils, a first measurement is done with the TMR sensor placed inside the coils but without the MEMS. Then, the MEMS is mounted on its PCB and the magnetic field detected by the TMR sensor is measured again. With both results, we calculate the modulation depth of the system, which is used as a figure of merit. Let us note that the objective is to obtain the biggest modulation depth possible, in order to improve the sensitivity of the system, and therefore the signal to noise ratio.

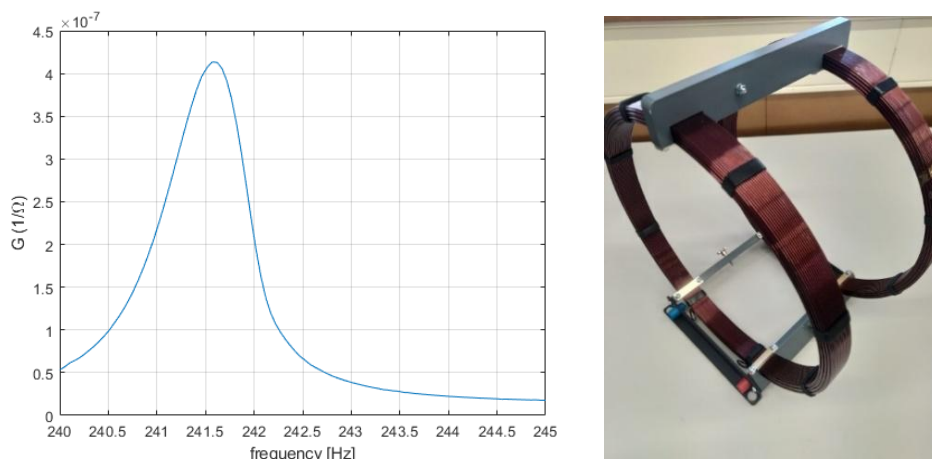


**Figure 38: MEMS conductance (Left), and Helmholtz coil (Right).**

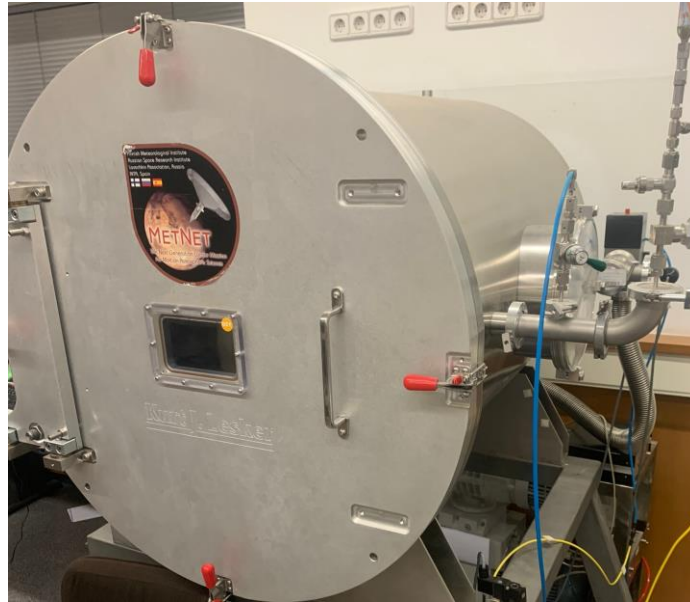


Figure 39: Vacuum chamber in UPC facilities.

Figure 40 shows an example of the experimental results obtained with a system that allows up to a successful 39% modulation depth to be achieved. Two spectra are provided: with and without MEMS.

$$e = 2 \frac{1.22657 \text{ uT}}{6.16252 \text{ uT}} = 39.8 \% \quad (7)$$

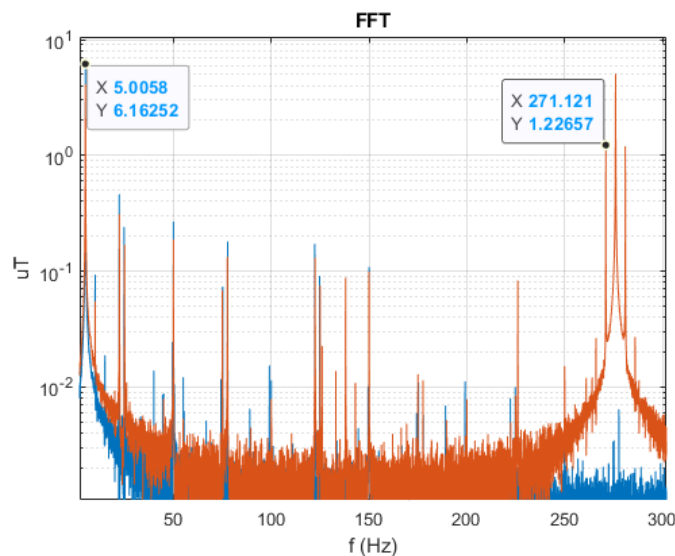


Figure 40: Fast Fourier Transform of the measurements done with MEMS (orange) and without MEMS (blue), of a system that delivers 39.8% of modulation depth.

## 7.2. Noise measurements

Noise measurements were firstly implemented in atmospheric conditions in the thermally stable cabin mentioned above. For further improvement of the results, subsequently, the setup was moved to a vacuum chamber. Results in both cases will be discussed.

It is important to say that for those measurements, another more thoroughly build and more characterized electronic system was adapted and used for the noise measurement, which was from the LETS project of the ICE (Institut Català del Espai).

### 7.2.1. Atmospheric pressure

Measurements with the system were done in atmospheric pressure in the thermally stable cabin. The MEMS was modulated with a sinusoidal signal with a frequency of 222.3 Hz and an amplitude of 3.3Vpp. The sensitivity for this MEMS, as it is the one used for the calibration, has the already presented value of 596.7 V/T.

The amplitude spectral density for the noise measurement with MEMS is depicted in Figure 41.

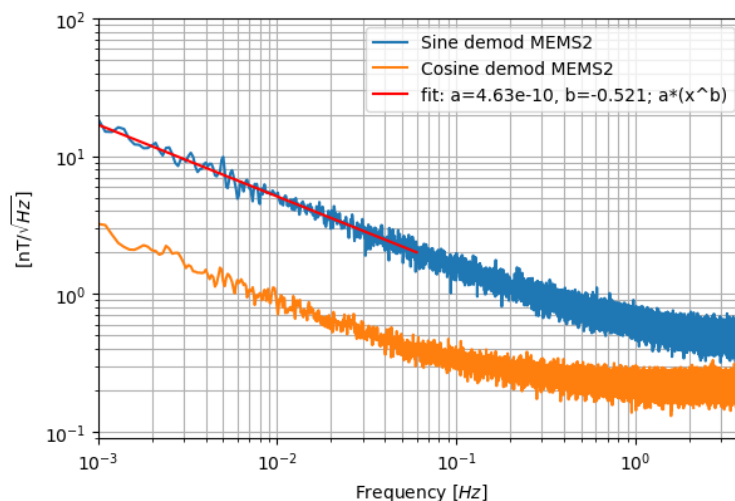


**Figure 41: Spectral density of the sinus demodulation and cosine demodulation of a measure with the complete system**

Using the fit represented in Figure 41, the noise level expected at a frequency of 0.1 mHz is approximately 60 nT/Hz. This result differs a factor 6 from the initial objectives of 10 nT/Hz at 0.1 mHz.

At low frequencies, below 1 Hz,  $1/f$ , noise appears that is phase-shifted in relation to the modulation signal causing it to become visible in both in-phase and quadrature demodulation. The origin of this noise is attributed to environmental disturbances.

### 7.2.2. Vacuum

In order to reduce the noise found at lower frequencies, the setup was moved into a vacuum chamber expecting to reduce the possible interferences with air and perform a better sensitivity with lower excitation voltages.

The measurements in the vacuum chamber were done with another system which had a higher sensitivity and was expected to have a better performance. The setup is the same as the one for the atmospheric pressure with the only difference that the mu-metal is set vertically, but no relevant difference is observed in changing its orientation. Figure 42 (left) shows the setup inside the vacuum chamber, whereas Figure 42 (right) shows the arrangement in the laboratory.

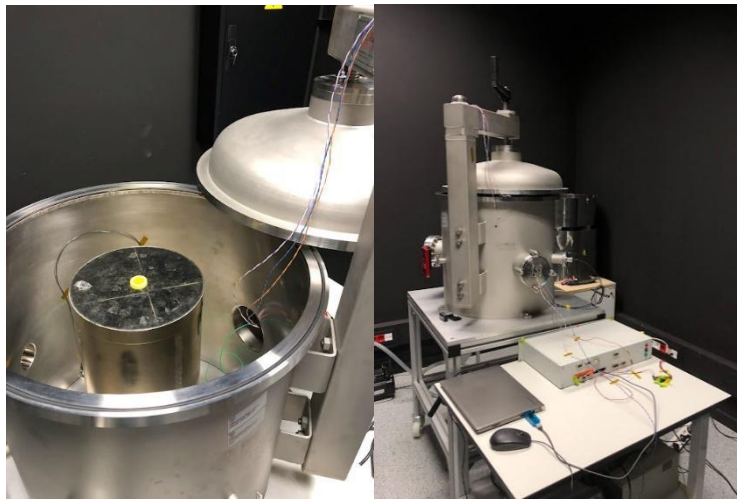


**Figure 42: Vacuum chamber with mu-chamber inside (left). Vacuum chamber sealed (right).**

The pressure reached in the vacuum chamber was  $1.9 \cdot 10^{-2}$  mBar. For this system, the resonance frequency and optimal amplitude for modulation, determined before the noise measurement, was 241.66 Hz with 650 mVpp, for the previous pressure and a given temperature.

Before and after each noise measurement sensitivity must be determined exactly the same way it was determined outside the vacuum. The sensitivity obtained before the measurement was 743.8 V/T and right after it, it had been reduced to 349.8 V/T. Due to this reduction, the sensitivity used for the amplitude spectral density is the mean of those previous values.

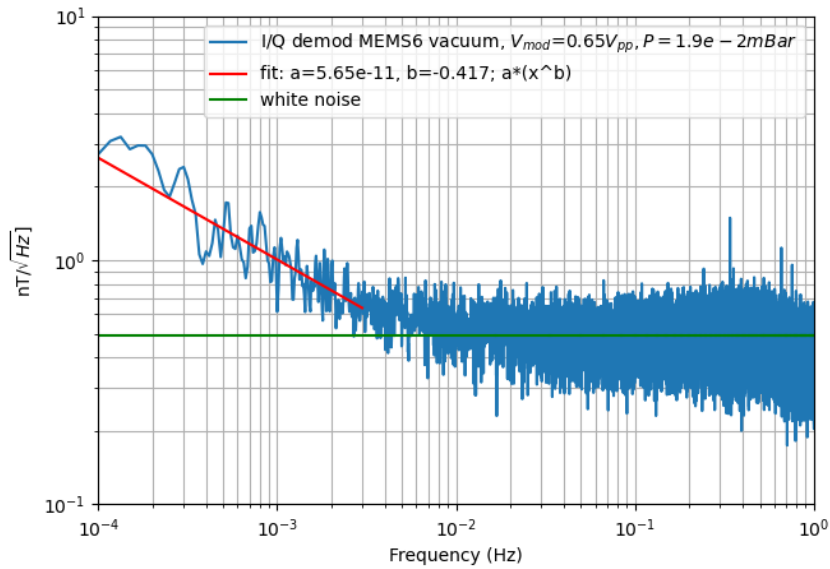


**Figure 43: Spectral density of the I/Q demodulation of a measurement with the complete system at vacuum.**

As shown in Figure 43, the results obtained fulfill the initial objective with approximately  $3 \text{ nT}/\sqrt{\text{Hz}}$  at 0.1mHz, even improving them with more than a factor of two. The  $1/f$  noise commented in the atmospheric pressure measurements still appears in the vacuum setup and it is attributed to some similar ambient factor. The noise floor of the sensor at higher frequencies is set to  $0.5 \text{ nT}/\sqrt{\text{Hz}}$ .

### 7.3. Device comparison

**Table 1: Comparison of the developed MEMS magnetometer to existing sensors for space exploration.**

	<i>This work</i>	<i>Insight fluxgate</i>	<i>Messenger fluxgate</i>	<i>Galileo fluxgate</i>	<i>Venus Express fluxgate</i>
<i>Miniaturized</i>	Yes	No	No	No	No
<i>Frequency Range</i>	0.1 mHz – 1Hz	10 mHz – 20 Hz	5 mHz – 100 mHz	0.1 mHz – 1 Hz	30 mHz – 300 mHz
<i>Noise Floor @ 0.1 mHz</i>	3 nT/√Hz	-	-	-	-
<i>Noise Floor @ 1 mHz</i>	1 nT/√Hz	-	-	-	-
<i>Noise Floor @10 mHz</i>	0.5 nT/√Hz	0.1 nT/√Hz	-	4.5 μT/√Hz	-
<i>Noise Floor @100 mHz</i>	0.5 nT/√Hz	0.1 nT/√Hz	20 pT/√Hz	-	396 μT/√Hz
<i>Noise Floor @1Hz</i>	0.5 nT/√Hz	0.1 nT/√Hz	-	0.2 μT/√Hz	-



Table 1 shows a comparison between the results obtained in this work and sensors used in different missions. Our sensor is compared to the magnetometers used in the missions Insight [5], Messenger [26], Galileo [27, 21] and Venus Express [28]. As shown, all of them are fluxgate sensors, therefore they are not miniaturized magnetometers. As it can be observed, the noise floor at different frequencies is close to the ones provided by the other sensors, while this work is the only one that can be fully miniaturized.

Additionally, the two orders of magnitude gained by modulating the magnetic field, instead of directly using the TMR, are essential for having noise floors similar to the ones of the other works.

## 8. Conclusions and future development

The requirements of the MELISA project have been successfully fulfilled:

- A noise floor below  $10nT/\sqrt{Hz}$  in the frequency range 0.1 mHz to 0.1 Hz has been achieved. The noise is  $3nT/\sqrt{Hz}$  in 0.1 mHz.
- A high modulation efficiency has been achieved, of 39%.

The results achieved indicate that, with further maturation of the technology, this technology can produce a low-power, compact and miniaturized magnetometer fulfilling for the observation of very low frequency magnetic field fluctuations.

It must be noted also that:

- The MEMS fabricated by MEMSCAP had a fabrication problem resulting in non-reliable resonators. The application of long-term actuation voltages very easily generates a short circuit in these devices. The reason acknowledged by the manufacturer was a problem during the etching of the oxide layer.

A new batch has been received, in which redesign techniques have been applied to avoid this issue, even in the case the same etching problem is detected. With the new batch we are currently being able to apply bigger voltages, and trying different approaches.

- The best system noise results have been obtained under vacuum. This way, it has been possible to increase the Q factor of the MEMS resonators, allowing large displacements with the application of low voltages. This last point has been important due to the fabrication problem mentioned before, since the long-time application of normal actuation voltages easily short-circuited the devices.

Additionally, it may also be possible that ambient pressure fluctuations are up-converted by the resonator, resulting in a  $1/f$  contribution after demodulation. The use of the devices under vacuum has been a key factor in the process of fulfilling the requirements. Further study of these causes is needed.

- It has not been possible to deposit thick high-permeability layers using sputtering or evaporation at the UPC clean room. The reason is that it was not possible to generate plasma in the sputtering, and the deposition velocity with evaporation was too slow. In order to overcome this problem, a mu-metal foil has been deposited on the structures. The thickness of this mu-metal layer is 20um.

## **Bibliography**

- [1] Hercik, D., et al (2017). The MASCOT Magnetometer. *Space Sci. Rev.*, 208(1), 433–449.
- [2] Tikoo, S. M., Evans, A. J. (2022). Dynamos in the Inner Solar System. *Annu. Rev. Earth Planet. Sci.*, 50(1), 99–122.
- [3] Johnson, C. L., et al (2020). Crustal and time-varying magnetic fields at the InSight landing site on Mars. *Nat. Geosci.*, 13(3), 199–204.
- [5] Banfield, D., Rodriguez-Manfredi, J. A., Russell, C. T., Rowe, K. M., Leneman, D., Lai, H. R., ...Team, T. T. (2018). In-Sight Auxiliary Payload Sensor Suite (APSS). *Space Sci. Rev.*, 215(1), 4–33.
- [6] Mittelholz, A., et al (2021), *J. Geophys. Res. Planets*, 126(11), e2021JE006980.
- [7] Johnson, C. L., et al (2020). *Nat. Geosci.*, 13(3), 199–204.
- [8] Du, Q., et al (2019). High Efficiency Magnetic Flux Modulation Structure for Magnetoresistance Sensor. *IEEE Electron Device Lett.*, 40(11), 1824–1827.
- [9] Tian, W., et al (2013). Magnetic Flux Vertical Motion Modulation for 1/ f Noise Suppression in Magnetoresistance Field Sensors Using MEMS Device. *IEEE Trans. Magn.*, 52(2), 1–6.
- [10] Li, X., et al (2018). A Novel High-Precision Digital Tunneling Magnetic Resistance-Type Sensor for the Nanosatellite Space Application. *Micromachines*, 9(3), 121.
- [11] Roberto Bruno, Daniele Telsoni, Danilo Delure, Ermanno Pietropaolo, Solar wind magnetic field background spectrum from fluid to kinetic scales, *Monthly Notices of the Royal Astronomical Society*, Vol 472, Issue 1 (2017)
- [12] Jawin, E. R., Valencia, S. N., Watkins, R. N., Crowell, J. M., Neal, C. R., & Schmidt, G. (2019). Lunar Science for Landed Missions Workshop Findings Report. *Earth Space Sci.*, 6(1), 2–40. doi: 10.1029/2018EA000490.
- [13] Brain, D. A. (2006). Mars Global Surveyor Measurements of the Martian Solar Wind Interaction. *Space Sci. Rev.*, 126(1), 77–112. doi: 10.1007/s11214-006-9122-x
- [14] Espley, J. R., Cloutier, P. A., Brain, D. A., Crider, D. H., & Acuña, M. H. (2004). Observations of low-frequency magnetic oscillations in the Martian magnetosheath, magnetic pileup region, and tail. *J. Geophys. Res. Space Phys.*, 109(A7). doi: 10.1029/2003JA010193
- [15] Connerney, J. E. P., Espley, J., Lawton, P., Murphy, S., Odom, J., Oliverson, R., & Sheppard, D. (2015). The MAVEN Magnetic Field Investigation. *Space Sci. Rev.*, 195(1), 257–291. doi: 10.1007/s11214-015-0169-4
- [1x] Ruhunusiri, S., Halekas, J. S., Espley, J. R., Mazelle, C., Brain, D., Harada, Y., ...Howes, G. G. (2017). Characterization of turbulence in the Mars plasma environment with MAVEN observations. *J. Geophys. Res. Space Phys.*, 122(1), 656–674. doi: 10.1002/2016JA023456
- [17] Johnson, C. L., Mittelholz, A., Langlais, B., Russell, C. T., Ansan, V., Banfield, D., ...Banerdt, W. B. (2020). Crustal and time-varying magnetic fields at the InSight landing site on Mars. *Nat. Geosci.*, 13(3), 199–204. doi: 10.1038/s41561-020-0537-x
- [18] James, M. K., Imber, S. M., Yeoman, T. K., & Bunce, E. J. (2019). Field Line Resonance in the Hermean Magnetosphere: Structure and Implications for Plasma Distribution. *J. Geophys. Res. Space Phys.*, 124(1), 211–228. doi: 10.1029/2018JA025920
- [19] Anderson, B. J., Acuña, M. H., Lohr, D. A., Scheifele, J., Raval, A., Korth, H., & Slavin, J. A. (2007). The Magnetometer Instrument on MESSENGER. *Space Sci. Rev.*, 131(1), 417–450. doi: 10.1007/s11214-007-9246-7
- [20] Tao, C., Sahraoui, F., Fontaine, D., de Patoul, J., Chust, T., Kasahara, S., & Retinò, A. (2015). Properties of Jupiter's magnetospheric turbulence observed by the Galileo spacecraft. *J. Geophys. Res. Space Phys.*, 120(4), 2477–2493. doi: 10.1002/2014JA020749
- [21] de Souza Echer, M. P., Echer, E., Domingues, M. O., Mendes, O., Seo, R. T., & Gonzalez, W. (2021). Wavelet analysis of low frequency magnetic field fluctuations in the Jupiter's magnetotail. *Adv. Space Res.*, 68(1), 246–258. doi: 10.1016/j.asr.2021.03.003
- [22] Russell, C. T., Snare, R. C., Means, J. D., & Elphic, R. C. (1980). Pioneer Venus Orbiter Fluxgate Magnetometer. *IEEE Trans. Geosci. Remote Sens.*, GE-18(1), 32–35. doi: 10.1109/TGRS.1980.350256

- [23] Guicking, L., Glassmeier, K.-H., Auster, H.-U., Delva, M., Motschmann, U., Narita, Y., & Zhang, T. L. (2010). Low-frequency magnetic field fluctuations in Venus' solar wind interaction region: Venus Express observations. *Ann. Geophys.*, 28(4), 951–967. doi: 10.5194/angeo-28-951-2010.
- [24] Dougherty, M. K., Kellock, S., Southwood, D. J., Balogh, A., Smith, E. J., Tsurutani, B. T., ...Cowley, S. W. H. (2004). The Cassini Magnetic Field Investigation. *Space Sci. Rev.*, 114(1), 331–383. doi: 10.1007/s11214-004-1432-2.
- [25] J. Valle et al. 'Design, Fabrication, Characterization and Reliability Study of CMOS-MEMS Lorentz-Force Magnetometers.' arXiv preprint, 2021. Doi: arXiv:2109.10980.
- [26] Anderson, B. J., Acuña, M. H., Lohr, D. A., Scheifele, J., Raval, A., Korth, H., Slavin, J. A. (2007). The Magnetometer Instrument on MESSENGER. *Space Sci. Rev.*, 131(1), 417–450. doi: 10.1007/s11214-007-9246-7
- [27] Tao, C., Sahraoui, F., Fontaine, D., de Patoul, J., Chust, T., Kasahara, S., Retin`o, A. (2015). Properties of Jupiter's magneto-spheric turbulence observed by the Galileo spacecraft. *J. Geophys. Res. Space Phys.*, 120(4), 2477–2493. doi: 10.1002/2014JA020749
- [28] Russell, C. T., Snare, R. C., Means, J. D., Elphic, R. C. (1980). Pioneer Venus Orbiter Fluxgate Magnetometer. *IEEE Trans. Geosci. Remote Sens.*, GE-18(1), 32–35. doi: 10.1109/TGRS.1980.350256
- [29] Du, Q., et al. (2020). Effect of magnetic flux modulation on noise characteristics of tunnel magnetoresistive sensors. *Appl. Phys. Lett.*, 116(10), 102405.

## Appendices

### MICROCONTROLLER CODE

\*It is important to know that this code was not entirely my work, a first version of this code was developed with the help of professor Vicente Jiménez.

```

/*****
0000000000.M E L I S A
Firmware for the MELISA circuit
Currently uses the F401 Board with mounted external XTAL
See Nucleo_401_Clock for the clock configuration details

SYSCLK 84 MHz
APB1 42 MHz
APB2 84 MHz

Hardware Pins

SPI1 (DAC) PA5(SCK) PA6(MISO) PA7(MOSI)
SPI2 (ADCs) PB13(SCK) PB14(MISO) PB15(MOSI)
SPI3 PC10(SCK) PC11(MISO) PC12(MOSI)
MCO2 PC9 (For testing)
SER2 PA2(TX) PA3(RX) Low Speed Text
SER PA9(TX) PA10(RX) High Speed Data
PWM PB4(CNV_LDAC)
CS PB6(DAC CS)
CS PC7(FTDI CS)

PRO PC8(PRO1) Hardware Profiling
TEST PB1(ADCCONV)

*****/

#include "mbed.h"
#include "arm_math.h"

#define SET_FLAG(var,flag) (var)=((var)|(flag))
#define CLEAR_FLAG(var,flag) (var)=((var)&~(flag))
#define CHECK_FLAG(var,flag) ((var)&(flag))

// PWM Synchronization configuration
#define SAMPLE_PERIOD 0.00001 // 10us Main period (100 KS/s)

#define SAMPLE_TIME_UP 0.000007 // 7us Time up for sample

// Sine generation configuration
// #define SINE_FREQ 1000 // 1kHz sine generation
// #define SINE_FREQ 255 // 223 Hz sine generation
#define SINE_FREQ 250 // 220.8 Hz sine generation

// #define Ncyc (int) 384
// //2147483648*Freq/100000
#define ANGLE_STEP ((double)(5368709.12))
// #define ANGLE_STEP ((int)(((1<<31)/N)))

// SPI1 configuration
// Bit Rate
// fapb2 is 84 MHz
// bit rate = fapb2 / 2^(BR+1)
// #define SPI1_BR 3 // 84 MHz / 2^4 = 5.25 MHz
#define SPI1_BR 2 // 84 MHz / 2^3 = 10.5 MHz
#define SPI1_CPOL 1 // Iddle clock state at 0 or 1 : Set to 1

```

```
#define SPI1_CPHA 1 // (0 first) (1 second) clock transition is active
#define SPI1_DFF 1 // (0 8 bit) (1 16 bit) data frame

// SPI2 configuration
// Bit Rate
// fapb1 is 42 MHz
// bit rate = fapb1 / 2^(BR+1)
##define SPI2_BR 2 // 42 MHz / 2^2 = 10.5 MHz
#define SPI2_BR 1 // 42 MHz / 2^2 = 10.5 MHz
#define SPI2_CPOL 0 // Idle clock state at 0 or 1 : Set to 1
#define SPI2_CPHA 0 // (0 first) (1 second) clock transition is active
#define SPI2_DFF 1 // (0 8 bit) (1 16 bit) data frame

// SPI3 configuration
// Bit Rate
// fapb1 is 42 MHz
// bit rate = fapb1 / 2^(BR+1)
##define SPI3_BR 2 // 42 MHz / 2^3 = 5.25 MHz
#define SPI3_BR 1 // 42 MHz / 2^2 = 10.5 MHz
#define SPI3_CPOL 0 // Idle clock state at 0 or 1 : Set to 1
#define SPI3_CPHA 0 // (0 first) (1 second) clock transition is active
#define SPI3_DFF 0 // (0 8 bit) (1 16 bit) data frame

// Board LED (Collision with SPI)
//DigitalOut myled(LED1);

//MCO2 at PC9
DigitalOut mco2(PC_9);

// Serial link with PC at 9600 baud
Serial pc(SERIAL_TX,SERIAL_RX);

// Serial link with PC at 9600 baud
Serial serData(PA_9,PA_10);

PwmOut cnvLdac(PB_4); // DAC/ADC synchronization TIMER 3 CH 1

// DAC CS
DigitalOut dacCS(PB_6);

//FTDI CS
DigitalOut ftdiCS(PC_7);

// ADC CONV for testing
DigitalOut adcCONV(PB_1);

// Gpio Test Lines
DigitalOut gtest1(PA_13);

// Profiling lines
DigitalOut PRO1(PC_8);
// Profiling code
#define PRO1_ON (GPIOC->ODR)|(1<<8)
#define PRO1_OFF (GPIOC->ODR)&=~(1<<8)

/***** LOW LEVEL GENERAL CODE *****/

// Precondition, port clock is active
void setAF(GPIO_TypeDef *port,int line,int af)
{
    int index,start;

    af = af&0xF; // Guarantee AF between 0 and 15

    // Informatin for AF Register
    index = line/8; // Register used 0 or 1
    start = 4*(line - index*8); // Position in this register
```

```
// Set GPIO line to AF function
port->MODER &= ~(1<<(line*2));
port->MODER |= (1<<(line*2+1));

// Set speed
//port->OSPEEDR |= (3<<(line*2)); // Set high speed

// Set alternate function number
port->AFR[index] &= ~(0xF<<start); // Erase AF information
port->AFR[index] |= (af<<start); // Set AF number
}

/***** CLOCK CODE *****/

// Shown information about the system clock
void clockInformation(void)
{
    int m,n,p,i;
    float f;

    pc.printf(" Clock information:\r\n");
    if ((RCC->CR) & (1<<0)) pc.printf(" HSI ON\r\n");
    if ((RCC->CR) & (1<<1)) pc.printf(" HSI Ready\r\n");
    if ((RCC->CR) & (1<<16)) pc.printf(" HSE ON\r\n");
    if ((RCC->CR) & (1<<17)) pc.printf(" HSE Ready\r\n");
    if ((RCC->CR) & (1<<18)) pc.printf(" HSE Bypass\r\n");
    if ((RCC->CR) & (1<<24)) pc.printf(" PLL Active\r\n");
    if ((RCC->CR) & (1<<25)) pc.printf(" PLL Locked\r\n");

    m = ((RCC->PLLCFGR) & 63);
    pc.printf(" PLL M = %d (divider to VCO input)\r\n",m);
    n = (((RCC->PLLCFGR)>>6) & 511);
    pc.printf(" PLL N = %d (multiplier)\r\n",n);
    i = (((RCC->PLLCFGR)>>16) & 3);
    switch(i)
    {
        case 0: p=2;
            break;
        case 1: p=4;
            break;
        case 2: p=6;
            break;
        case 3: p=8;
            break;
    }
    pc.printf(" PLL P = %d (output divider)\r\n",p);

    if ((RCC->PLLCFGR) & (1<<22))
        pc.printf(" PLL source is HSE\r\n");
    else
        pc.printf(" PLL source is HSI\r\n");

    f = 1.0f*n/m/p;
    pc.printf(" PLL total multiplication = %f\r\n",f);
    pc.printf(" Clock source is ");
    switch (((RCC->CFGR)>>2)&3)
    {
        case 0: pc.printf("HSI\r\n");
            break;
        case 1: pc.printf("HSE\r\n");
            break;
        case 2: pc.printf("PLL\r\n");
            break;
        case 3: pc.printf("(Cannot be)\r\n");
            break;
    }
}
```

```

    }
    pc.printf("\r\n"); // Blank line
}

// Send sysClk/5 to the MCO2 pin PC9
void activateMCO2(void)
{
    // Select main clk
    CLEAR_FLAG((RCC->CFGR),(3u<<30));
    // Select :5 divider
    SET_FLAG((RCC->CFGR),(7<<27));
    // Set maximum frequency on PC9
    SET_FLAG((GPIOC->OSPEEDR),(3<<18));
    // Set alternate function on PC9
    CLEAR_FLAG((GPIOC->MODER),(1<<18));
    SET_FLAG((GPIOC->MODER),(1<<19));
    // Set Alternate function PC9 to 0000
    CLEAR_FLAG((GPIOC->AFR[1]),(15<<4));
}

// Change to HSE
void changeHSE(void)
{
    // Change system clock to HSI
    CLEAR_FLAG((RCC->CFGR),3);

    // Wait for change to be effective
    while (CHECK_FLAG((RCC->CFGR),3)!=0) {};

    // Disable PLL
    CLEAR_FLAG((RCC->CR),(1<<24));

    // Change PLL M
    CLEAR_FLAG((RCC->PLLCFGR),63); // Set 8 value
    SET_FLAG((RCC->PLLCFGR),8);

    // Set PLL source to HSE
    SET_FLAG((RCC->PLLCFGR),(1<<22));

    // Enable PLL
    SET_FLAG((RCC->CR),(1<<24));

    // Change system clock to PLL
    SET_FLAG((RCC->CFGR),(1<<1));

    // Wait for change to be effective
    while (CHECK_FLAG((RCC->CFGR),3)!=2) {};
}

void configureClock(void)
{
    // Activate HSE
    SET_FLAG((RCC->CR),(1<<16));
    wait(1.0);

    changeHSE();

    // Show clock information
    clockInformation();

    // Put sysclk/5 on PC9
    activateMCO2();
}

/** SPI Code *****/

void configureSPI(void)

```

```

{
// SPI1 configuration
RCC->APB2ENR |= (1<<12); // Activate SPI1 clock
RCC->APB1ENR |= (1<<14); // Activate SPI2 clock
RCC->APB1ENR |= (1<<15); // Activate SPI3 clock

RCC->AHB1ENR |= (1); // Activate GPIO A
RCC->AHB1ENR |= (1<<1); // Activate GPIO B
RCC->AHB1ENR |= (1<<2); // Activate GPIO C

// Configure SPI1
// Set BR value
SPI1->CR1 = ((SPI1_BR)&7)<<3;
// Set CPOL value
SPI1->CR1 |= (SPI1_CPOL)<<1;
// Set CPHA value
SPI1->CR1 |= (SPI1_CPHA);
// Set DFF value
SPI1->CR1 |= (SPI1_DFF)<<11;
// Set SSM and SS
SPI1->CR1 |= (1<<9)|(1<<8);
// Activate SPI1 in master mode
SPI1->CR1 |= (1<<2)|(1<<6);

// Pins used are PA5, PA6, PA7 at AF05
setAF(GPIOA,5,5);
setAF(GPIOA,6,5);
setAF(GPIOA,7,5);

// Configure SPI2
// Set BR value
SPI2->CR1 = ((SPI2_BR)&7)<<3;
// Set CPOL value
SPI2->CR1 |= (SPI2_CPOL)<<1;
// Set CPHA value
SPI2->CR1 |= (SPI2_CPHA);
// Set DFF value
SPI2->CR1 |= (SPI2_DFF)<<11;
// Set SSM and SS
SPI2->CR1 |= (1<<9)|(1<<8);
// Activate SPI2 in master mode
SPI2->CR1 |= (1<<2)|(1<<6);

// Pins used are PB13, PB14, PB15 at AF05
setAF(GPIOB,13,5);
setAF(GPIOB,14,5);
setAF(GPIOB,15,5);

// Configure SPI3
// Set BR value
SPI3->CR1 = ((SPI3_BR)&7)<<3;
// Set CPOL value
SPI3->CR1 |= (SPI3_CPOL)<<1;
// Set CPHA value
SPI3->CR1 |= (SPI3_CPHA);
// Set DFF value
SPI3->CR1 |= (SPI3_DFF)<<11;
// Set SSM and SS
SPI3->CR1 |= (1<<9)|(1<<8);
// Activate SPI3 in master mode
SPI3->CR1 |= (1<<2)|(1<<6);

RCC->AHB1ENR |= (1<<2);
GPIOC->OSPEEDR |= (3<<20)|(3<<22)|(3<<24);

// Pins used are PC10, PC11, PC12 at AF06
setAF(GPIOC,10,6);

```

```

setAF(GPIOC,11,6);
setAF(GPIOC,12,6);

//GPIOC->OSPEEDR |= (3<<20)|(3<<22)|(3<<24);

// Initialize CS lines
dacCS = 1;
ftdiCS = 1;
}

int SPIsend(int data1,int data2,int data3)
{
volatile int i,j=0;

SPI1->DR = data1;
SPI2->DR = data2;
SPI3->DR = data3;

wait_us(1);
//for(i=0;i<100000;i++) j++;

while (!((SPI1->SR) & 1));
while (!((SPI2->SR) & 1));
while (!((SPI3->SR) & 1));
return 0;
}

int SPI1send(int data)
{
SPI1->DR = data;

wait_us(1);
//for(i=0;i<100000;i++) j++;

while (!((SPI1->SR) & 1));
return 0;
}

int SPI2receive(void)
{
int data;

SPI2->DR = 0;

wait_us(1);
//for(i=0;i<100000;i++) j++;

while (!((SPI2->SR) & 1));

data = SPI2->DR;

return data;
}

// Configure the dac/adc sync signal
void configurePWM(void)
{
cnvLdac.period(SAMPLE_PERIOD);
cnvLdac.write(SAMPLE_TIME_UP/SAMPLE_PERIOD);
}

/***** KERNEL *****/
void kernel_float(void)
{
double angle = 0;
int32_t dacData;          // Data for DAC

```

```

volatile int32_t v1=124,v2; // Dummy vars for small delays
int32_t adc1=0,adc2=0; // ADC data
int32_t data1,data2,data3,data4; // Data to send
int32_t cycle = 0;

//Envio una de cada N_diff
float N_diff=4;
float N_diff_new=N_diff;
int32_t N=0;

while(1) // Main loop
{
// Time = 0us
while(TIM3->CNT) {}; // Sync to timer start

//Lectura dels ADCs
data1 = (adc1>>8)&0xFF; //MSB
data2 = adc1&0xFF; //LSB
if (data2 == 0) data2 = 1;
data3 = (adc2>>8)&0xFF; //MSB
data4 = adc2&0xFF; //LSB
if (data4 == 0) data4 = 1;

// Framing synchronization for FTDI!!! and For the framing values!

N=N+1;
if(N>=N_diff_new){
cycle++;
if (cycle == 100) cycle = 0;
N=0;
}

dacCS = 0; // Activate DAC CS

//
if(N==0)ftdiCS = 0; // Activate FTDI CS

// Compute new angle for DAC during ADC measurement

angle = (angle + ANGLE_STEP);
if(angle>2147483648){
angle=angle-2147483648;
}
dacData = (1<<15)+(arm_sin_q31((int)angle)/(1<<17))*1470/1000;//->mVpp

// Time = 0.76 us

// Delay before reading ADC data
for(v1=0;v1<2;v1++)
v2 = arm_sin_q31(v1);

// Time = 1.76 us
PRO1_ON; // Activate profiling line

SPI2->DR = 0; // Start receiving ADC1 data
SPI1->DR = dacData; // Start Sending DAC data

//FTDI!!
if(N==0)SPI3->DR = data1; // ADC#1(msb)

// Delay before checking transfer end
v2 = arm_sin_q31(v1);

// Check busy flag for FTDI!!
if(N==0)while ((SPI3->SR)&(1<<7));

```

```

// Time = 2.94 us
//TFDI!!
if(N==0)SPI3->DR = data2; // ADC#1(lsb)

// Delay before checking transfer end
v2 = arm_sin_q31(v1);

//FTD!!!
// Check busy flag for FTDI
if(N==0)while ((SPI3->SR)&(1<<7));

// Check busy flag for ADC
while ((SPI2->SR)&(1<<7));

// Time = 4.12 us

// Get ADC1 reading
adc1 = SPI2->DR;

SPI2->DR = 0; // Start receiving ADC2 data
//TFD!!!
if(N==0)SPI3->DR = data3; // ADC#2(LSB)

// Delay before checking transfer end
v2 = arm_sin_q31(v1);

//FTD!!!!
// Check busy flag for FTDI
if(N==0)while ((SPI3->SR)&(1<<7));

// Time = 5.26 us
//FTD!!!
if(N==0)SPI3->DR = data4; // ADC#2(MSB)

// Delay before checking transfer end
v2 = arm_sin_q31(v1);

//FTD!!!!
// Check busy flag for FTDI
if(N==0)while ((SPI3->SR)&(1<<7));

// Check busy flag for ADC
// We don't need to check DAC EOT as it sure has ended at this point
while ((SPI2->SR)&(1<<7));

// Time = 6.4 us

// Get ADC2 reading
adc2 = SPI2->DR;

PRO1_OFF; // Deactivate profiling line

dacCS = 1; // Deactivate DAC CS

// Convert received data to signed integer
if (adc1>0x7FFF) adc1 = -0x10000 + adc1;
if (adc2>0x7FFF) adc2 = -0x10000 + adc2;

// Convert to unsigned
adc1 += (1<<15);
adc2 += (1<<15);

//data1old=data1;
//data2old=data2;
//data3old=data3;
//data4old=data4;

```

```

// Send framing data if needed
//FTDI!!!!
if(N==0)
{
if (!cycle)
{
SPI3->DR = 0;

// Delay before checking transfer end
v2 = arm_sin_q31(v1);

// Check busy flag for FTDI
while ((SPI3->SR)&(1<<7));

SPI3->DR = 0;

// Delay before checking transfer end
v2 = arm_sin_q31(v1);

// Check busy flag for FTDI
while ((SPI3->SR)&(1<<7));
}

ftdiCS = 1; // Disable CS
}
//END FTDI
}

}

/*****/

int main()
{
pc.printf("\r\n===== \r\n");
pc.printf(" MELISA Firmware (Ver %s)\r\n",VERSION);
pc.printf("===== \r\n\r\n");

// Configure Clock to use external XTAL
// configureClock();
// Configure PWM sync signal
configurePWM();

// Set serial 1 baud
serData.baud(5000000);

// Configure the SPI peripherals
configureSPI();

// Execute kernel (Never returns)
kernel_float();

// Without blink
while(1)
{
wait(0.2); // 1 sec
serData.printf("A");
SPIsend(0x5555,0x5555,0x5555);
}
}

```

## PYTHON ACQUISITION CODE

### MICROCONTROLLER CODE

It is important to know that this code was not entirely my work, a first version of this code was developed with the help of professor Vicente Jiménez.

```
# MELISA PROCESSING CODE
# Current Version
# Xavier Manyosa i Vilardell
#Millores de la versió:
#Multiprocessing using PIPES
# Imports
from multiprocessing import Process, Pipe
import time
import numpy as np
#import math
import ft4222
import sys
import signal

#####
##### Processes #####
#####

def signal_handler(signal, frame):
    global dev

    dev.close()
    sys.exit(-1)

def worker(conn,val):

    nom_fitxer="C:\\Users\\mntuser\\Desktop\\Xavi\\MELISA CODE\\Output\\"+str(val)+".txt"#Output file name
    file_object=open(nom_fitxer,'w')

    index=0
    nb=0
    QuarterSignalLength=25;
    #Buffer excitació
    buffer_exc=np.zeros(QuarterSignalLength+1)

    #delmat=20 #S'agafata una de cada "delmat" samples
    buffer_size=20

    #Buffers per al filtre
    Input_buffer_q=np.zeros(3, dtype=np.double)
    Output_buffer_q=np.zeros(3, dtype=np.double)#Output Buffer
    Input_buffer_i=np.zeros(3, dtype=np.double)
    Output_buffer_i=np.zeros(3, dtype=np.double)#Output Buffer

    #Filter Coefficients
    #100kS/s
    #Num_b=np.array([0.246685308301432e-7, 0.493370616602863e-7, 0.246685308301432e-7], dtype=np.double)
    #Den_a=np.array([1, (-1.999555711713490), 0.999555810387614], dtype=np.double)
    #10kS/s
    #Num_b=np.array([2.46193004641367e-06, 4.92386009282734e-06, 2.46193004641367e-06], dtype=np.double)
    #Den_a=np.array([1, (-1.99555712434579), 0.995566972065975], dtype=np.double)

    #Num_b=3.66676642496026e-06    7.33353284992053e-06    3.66676642496026e-06
    #Den_a=1    -1.99457657215307    0.994591239218773

    while True:
        values = conn.recv()
```

```

#print('Després de rebre pel Proc')
for i in range(buffer_size):#0 to buffer size - 1

    buffer_exc[nb]=values[1][i]

    ##### 1.- DEMODULATION #####
    if (index==0):
        Input_buffer_q[0]=values[0][i]*values[1][i]
        if(nb==QuarterSignalLength):#en aquest cas necessito el 0
            Input_buffer_i[0]=values[0][i]*buffer_exc[0]
        else:
            Input_buffer_i[0]=values[0][i]*buffer_exc[nb+1]

        Output_buffer_i[0]=Input_buffer_i[0]*3.94433639686588e-07 + Input_buffer_i[2]*7.88867279373177e-
07+Input_buffer_i[1]*3.94433639686588e-07- Output_buffer_i[2]*(-1.998222847291842)-
Output_buffer_i[1]*0.998224425026401
        Output_buffer_q[0]=Input_buffer_q[0]*3.94433639686588e-07 + Input_buffer_q[2]*7.88867279373177e-
07+Input_buffer_q[1]*3.94433639686588e-07- Output_buffer_q[2]*(-1.998222847291842)-
Output_buffer_q[1]*0.998224425026401

        index=1
    elif(index==1):
        Input_buffer_q[1]=values[0][i]*values[1][i]
        if(nb==QuarterSignalLength):#en aquest cas necessito el 0
            Input_buffer_i[1]=values[0][i]*buffer_exc[0]
        else:
            Input_buffer_i[1]=values[0][i]*buffer_exc[nb+1]

        Output_buffer_i[1]=Input_buffer_i[1]*3.94433639686588e-07 + Input_buffer_i[0]*7.88867279373177e-
07+Input_buffer_i[2]*3.94433639686588e-07- Output_buffer_i[0]*(-1.998222847291842)-
Output_buffer_i[2]*0.998224425026401
        Output_buffer_q[1]=Input_buffer_q[1]*3.94433639686588e-07 + Input_buffer_q[0]*7.88867279373177e-
07+Input_buffer_q[2]*3.94433639686588e-07- Output_buffer_q[0]*(-1.998222847291842)-
Output_buffer_q[2]*0.998224425026401

        index=2
    elif(index==2):
        Input_buffer_q[2]=values[0][i]*values[1][i]
        if(nb==QuarterSignalLength):#en aquest cas necessito el 0
            Input_buffer_i[2]=values[0][i]*buffer_exc[0]
        else:
            Input_buffer_i[2]=values[0][i]*buffer_exc[nb+1]

        Output_buffer_i[2]=Input_buffer_i[2]*3.94433639686588e-07 + Input_buffer_i[1]*7.88867279373177e-
07+Input_buffer_i[0]*3.94433639686588e-07- Output_buffer_i[1]*(-1.998222847291842)-
Output_buffer_i[0]*0.998224425026401
        Output_buffer_q[2]=Input_buffer_q[2]*3.94433639686588e-07 + Input_buffer_q[1]*7.88867279373177e-
07+Input_buffer_q[0]*3.94433639686588e-07- Output_buffer_q[1]*(-1.998222847291842)-
Output_buffer_q[0]*0.998224425026401

        index=0
        ##### Save to .txt and update index #prova#####

        nb=nb+1
        if(nb==QuarterSignalLength+1):
            nb=0;
            file_object.write(f"{Output_buffer_q[index]}\t{Output_buffer_i[index]}\n")
        #print('Dades Processades')

```

```
if __name__ == '__main__':
#####
##### Initi #####
#####

#nom_fitxer="C:\\Users\\mntuser\\Desktop\\Xavi\\MELISA CODE\\Output\\prova.txt" #Output file name
#file_object2=open(nom_fitxer,'w')

#Fs=24038 #Sampling Frequency

Periods_signal=20
Vref=3.3
pi=3.14159

# Set maximum clock frequency for FTDI device
ft4222.SysClock(3)

# open device with default description 'FT4222 A'
dev = ft4222.openByDescription('FT4222 A')
#Inicio el device
dev.spiSlave_InitEx(1)
#Creo el process i la connexió amb pipe

parent_conn, child_conn = Pipe()
val = input("Enter the name of the file: ")
p = Process(target=worker, args=(child_conn,val,))
p.start()
buffer_size=20

#Buffers on va a parar la raw data adquirida pels ADCs
buffer_exc=np.zeros(buffer_size)#Buffer 1 with excitation data
buffer_mod=np.zeros(buffer_size)#Buffer 1 with modulated data

#####
##### Wait for the framing #####
#####
signal.signal(signal.SIGINT, signal_handler)
# Wait a little after initialization
time.sleep(2)
# Wait for 0 0 framing
frame = 0
count = 0
print("Esperant al framing")

while frame == 0: # Si el frame encara no s'ha llegit
    data = dev.spiSlave_Read(1) #Espero a llegir la propera dada
    if data: #Si he rebut la dada
        if ord(data) == 0: #Si la dada és igual a 0
            count = count + 1 #Sumo un
            if count == 2: #Si ja he rebut dos 0 seguits
                frame = 1 #Ja tinc el frame, per tant, no torno a entrar
        else:
            count = 0 #Si rebo quelcom diferent a 0, resetejo el count
print("Ja té el framing")

#####
##### MAIN #####
#####
```

```

nread = 0
zoneCount = 0
stepCounter = 0
count = 0
phase = 0
lastData = -1
t=0.0
adc1=0
adc2=0
mod=0
lastData = dev.spiSlave_Read(1)
n=0
while True: #Durant el temps de lectura
    data = dev.spiSlave_Read(1) #Llegeixo la dada
    if data: #Si hem llegit una dada
        #Processat de les dades
        #if ord(data)==0:
            #print("Un zero a:", zoneCount)
            #if (zoneCount%2)==1:
                #print("A més sóc senar:", zoneCount)
        if ord(data) == 0 and lastData == 0: # Rebo dos bytes de framing
            lastData=-1
            phase = 0
            count = 0
            if not zoneCount == 401: # He perdut algun byte en aquest framing passat?
                print("Error: Zone mismatch!" )
                print("Count:",zoneCount)
                #file_object_2.write("Error:zone mismatch'+"\n")
            zoneCount = 0
            #Comença el processat
        else:
            lastData = ord(data)
            zoneCount = zoneCount+1
            if count == 0: # Si és el primer byte d'un ADC
                data1= ord(data)<<8 # L'agafo i el multiplico per 256 (MSB)

            else:
                data1=data1+ord(data) # Si és el segon li sumo al primer multiplicat per 256(MSB)
                #data1=(((data1-32768)/32767)*Vref) # El passo a Volts
                data1=(((data1-32768)*1.007110812707e-4) # El passo a Volts
            if phase: #Si phase és igual a 1, és a dir ja tenim les dades del segon adc
                #data1=buffer_exc[n]*0.1*math.sin(6.2831853*t)#simulo la adquisició de la senyal modulada
                phase = 0 #De manera que després ve el adc1
                ##Aquí passem els valors!
                buffer_mod[n]=data1
                #if 0==n%20:
                    #file_object2.write(f"{buffer_mod[n]}\t{buffer_exc[n]}\n")
                    #file_object2.write(f"{buffer_mod[n]}\n")
                    #file_object2.write(f"{buffer_mod[n]}\t{buffer_exc[n]}\n")
                n=n+1;
            if n==buffer_size:
                n=0
                #Comentar si només vull raw
                parent_conn.send([buffer_mod, buffer_exc])
            else: # Si és el torn del primer ADC
                phase = 1
                buffer_exc[n]=data1

```



```
if count == 0:  
    count = 1  
else:  
    count=0  
#Acaba el processat  
p.join()
```



## **Glossary**

MEMS: Microelectromechanical System

ADC: Analog to Digital Converter

DAC: Digital to Analog Converter

TMR: Tunneling Magnetic Resistor

MFC: Magnetic Flux Concentrator

MTJ: Magnetic Tunnel Junction

LISA: Laser Interferometer Space Antenna

LEO: Low Earth Orbit

FEM: Finite Element Methods (simulations)

PCB: Printed Circuit board

FTDI: Chip to ensure fast communication between a PC and a microcontroller

MR: Magnetoresistance

SPI: Serial peripheral interface

MCU: Microcontroller Unit

SWD: Serial Wire Debug

ISP: In system Programming